Defect-induced fracture topologies in Al_2O_3 ceramic-graphene nanocomposites

Materials & Design 239 (2024) 112783

Contents lists available at ScienceDirect

Materials & Design

journal homepage: www.elsevier.com/locate/matdes

Defect-induced fracture topologies in Al_2O_3 ceramic-graphene nanocomposites

E.N. Borodin [a,*], A.G. Sheinerman [b], O.Yu. Bushuev [a], M.Yu. Gutkin [b], A.P. Jivkov [a]

[a] Department of Solids and Structures, School of Engineering, The University of Manchester, Manchester M13 9PL, UK
[b] Institute for Problems in Mechanical Engineering of the Russian Academy of Sciences, Bolshoj 61, Vasil. Ostrov, St. Petersburg 199178, Russia

ARTICLE INFO

Keywords:
Ceramic fracture
Nanocomposites
Reduced graphene oxide
rGO
Fracture network topology
Materials design
Fracture resistance
Polytopal cell complex
Algebraic topology
Nanocrystalline materials

ABSTRACT

Models of ceramic-graphene nanocomposites are used to study how the manufacturing process-dependent arrangement of reduced graphene oxide (rGO) inclusions governs nano-crack network development. The work builds upon recent studies of such composites where a novel combinatorial approach was used to investigate the effect of rGO arrangements on electrical conductivity and porosity. This approach considers explicitly the discrete structure of the composite and represents it as a collection of entities of different dimensions - grains, grain boundaries, triple junctions, and quadruple points. Here, the combinatorial approach is developed further by considering the effects of rGO agglomerations, stress concentrators and adhesion energies on intergranular cracking. The results show that the fracture networks can be effectively controlled by the local ordering of rGO inclusions to allow for a concurrent increase in the strength and conductivity of the ceramic composites. It is shown that the ratio of local stress concentrators related to rGO inclusions and cracks is the most significant factor affecting the nano-crack network topology. The local spatial arrangement of rGO inclusions becomes an effective tool for controlling nano-crack network topology only when this ratio approaches one. It is anticipated that these results will inform future design of toughness-enhanced composites.

List of the used abbreviations and model variables

IFN	induced fracture network
ISC	local stress concentrators related to inclusions
CSC	local stress concentrators related to nanocracks
rGO	reduced graphene oxide
PCC	polytopal cell complex
GB	grain boundary
TJ	triple junction
QP	quadruple point
$\mathcal{T}$	tessellation of a 3-dimensional space by polyhedra
$\mathcal{M}$	PCC based on a tessellation $\mathcal{T}$
$\mathcal{M}_k$	k-skeleton of a PCC
p, f	fractions of inclusions and nanocracks, respectively
p_a	fraction of GBs containing agglomerations of inclusions
p_m, p_v	mass and volume fractions of rGO powder in a composite
J^r_ω, J^c_ω	triple junction ω-types corresponding to $\omega \in \{0,1,2,3\}$ rGO inclusions and nanocracks on their co-boundary
j^r_ω, j^c_ω	fraction of ω-type triple junctions containing inclusions and nanocracks
D_k	triple junction d-type corresponding to $k \in \{1,2,3\}$ incident GBs of the same type in the network of inclusions or nanocracks
d^r_k, d^c_k	fraction of k-type triple junctions containing inclusions and nanocracks
B_L, C_L	grain boundary indices of inclusions and nanoracks, respectively
S^r_{conf}, S^c_{conf}	TJ configuration entropies of inclusions and nanocracks, respectively
∂_k, δ_k	full incidence matrices of k-cells and their transposed counterparts
$\widehat{\partial}_k, \widehat{\delta}_k$	reduced incidence matrices of k-cells and their transposed counterparts
$L_k, \widehat{L_k}$	full and reduced k-th combinatorial Laplacian of a PCC
Γ_m,	energy of ceramic matrix boundaries
Γ_r,	energy of grain boundaries containing graphene inclusions

* Corresponding author.
E-mail address: elbor7@gmail.com (E.N. Borodin).

https://doi.org/10.1016/j.matdes.2024.112783
Received 6 November 2023; Received in revised form 14 February 2024; Accepted 19 February 2024
Available online 23 February 2024

Γ_a,	energy of grain boundary agglomerations having rGO-rGO bounds
Σ_r,	adhesion energy of the matrix-rGO grain boundaries
Σ_m,	adhesion energy of the matrix-matrix grain boundaries
Σ_a,	adhesion energy of the grain boundaries containing agglomeration
E_{rl}, E_{cl},	elastic energies of local stress concentrators related to inclusions and nanocracks, respectively
η_r, η_c,	coefficients determining CSC and ISC
W_b,	topological grain boundary weight

1. Introduction

Brittle composites, such as polycrystalline ceramics, have low resistance to cracking. Inclusions in ceramics are often used for improving a physical property. For example, the electrical conductivity can be increased by the introduction of highly-conductive inclusions in the low-conductive ceramic matrices. This is considered in the design of novel metal oxide electro-mechanical composites with inclusions of reduced graphene oxide (rGO) [1,2], and in graphene-enriched ceramics [3–12] which are candidates for advanced energy storage materials [1]. It has been suggested that the introduction of soft two-dimensional (2D) highly conductive inclusions into a three-dimensional (3D) hard ceramic matrix creates a composite with a unique combination of electrical [5,6,10,12,13], thermal [14], and mechanical [2,4,7,10,11,15] properties. In different modifications, graphene-ceramic composites can be utilised as the new catalyst promising for its applications in low-temperature fuel cells [16] or membrane nano-filters made of alumina nano-composite [17] useful for drinking water decontamination and other biotechnological applications [18]. Among their other applications are surface renewable electrodes [19], energy storage materials, electronic devices [19], and bioceramic scaffolds with reinforced osteoinductivity [20]. All these applications benefit from the synergy of the corresponding functional (electrical, chemical, biological) properties and mechanical resilience to fracture [21,22]. However, it is generally expected that the addition of inclusions, which can be viewed as initial matrix damage, would decrease further the apparent fracture toughness and thus reduce the load-baring capacity of the composite. Increasing the resistance of ceramic composites to cracking is a significant challenge, which must be addressed to facilitate the effective use of ceramic composites in many critical areas. Some recent works [3–6] have shown that an advanced design, which accounts not only for the fraction of inclusions and their types but also for their spatial arrangements [3,4], can improve simultaneously the strength and the electrical conductivity.

From a different perspective, cracking is the main energy dissipation mechanism in brittle materials [23]. It increases their dynamic strength, which makes the development of fractal-like crack networks desirable in many automotive, defence, and aerospace applications. Because cracking in brittle polycrystalline materials is predominantly intergranular, i.e., along grain boundaries (GBs), decreasing the grain size down to the nano-meter range would increase significantly the energy dissipation capacity of a fracture network. Arrangement of 2D defects on GBs, attached to grains with weak adhesive forces [24], could be a suitable approach for managing the development of fracture network that optimises both the energy dissipation and the load-bearing capacity of the composite. The design of optimal arrangements requires an approach for relating arrangement characteristics and energy dissipation capacity of the network of micro- and nano-cracks. The commonly used continuous and mesoscale approaches [25,26] are not able to meet this requirement. A novel discrete approach based on the representation of polycrystalline materials as combinatorial cell complexes, developed recently [27,28], makes it possible to analyse the effect of defect distributions and their multi-dimensional interactions [3,4] on the materials fracture parameters.

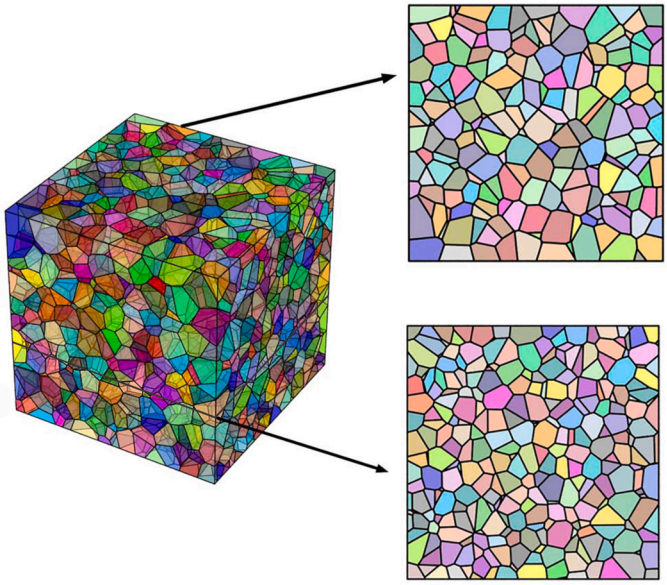

Fig. 1. Voronoi tessellation of a cube constructed by Neper [32], with two planar cuts.

The aim of this work is to understand better and describe the fracture development in graphene-ceramic nanocomposites, which have been previously shown to exhibit excellent electrical and strength properties, but have not been optimised for fracture resistance via inclusions arrangement. The study material is Al_2O_3 ceramic composite with rGO inclusions. The method for description and topological analysis of polycrystalline assemblies, viewed as collections of discrete entities with different dimensions, is outlined in Section 2. The computational results based on the method are presented in Section 3, together with a discussion on the relationships between the arrangements of rGO inclusions and the fracture networks developing under the action of external loads. The results support a conclusion on the critical factor for composite strength and a choice of optimal design strategy between: (i) decreasing the number of agglomerations of inclusions, which are weak spots for fracture initiation and (ii) decreasing the number of stress concentrators at triple junctions of grain boundaries. The study is focused on the effect of stress concentrators, while any dynamic features are neglected.

2. Methods for description and analysis of ceramic composites

2.1. Ceramic composites as polytopal cell complexes

The mathematical description of composites follows the works [3, 27–29]. The microstructure is considered as a collection of connected elements of different dimensions: 3D *grains*, 2D *grain boundaries* (GBs), 1D *triple junctions* (TJs) [30], and 0D *quadruple points* (QPs) [31].

A model microstructure is created by tessellating a given spatial domain into convex polytopes so that the shapes and sizes of the polytopes represent statistically the elements of a real microstructure [1,5,6]. The free open-source software Neper [32] is used in this work to create Voronoi tessellations of spatial domains [33,34], which provide reliable representations of microstructures [35]. A tessellation, $\mathcal{T}$, contains *polyhedrons*, i.e., 3D polytopes representing grains, *faces*, i.e., 2D polytopes representing GBs, *edges*, i.e., 1D polytopes representing TJs, and *nodes*, i.e., 0D polytopes representing QPs. In the language of algebraic topology, the polytopes of dimension k are referred to as *k-cells* and $\mathcal{T}$ is referred to as a polytopal cell complex (PCC) [36,37]. Fig. 1 shows a tessellation of a cube containing 3,000 3-cells (grains), 22,057 2-cells (GBs), 38,116 1-cells (TJs) and 19,060 0-cells (QPs), together with two planar cuts for future reference.

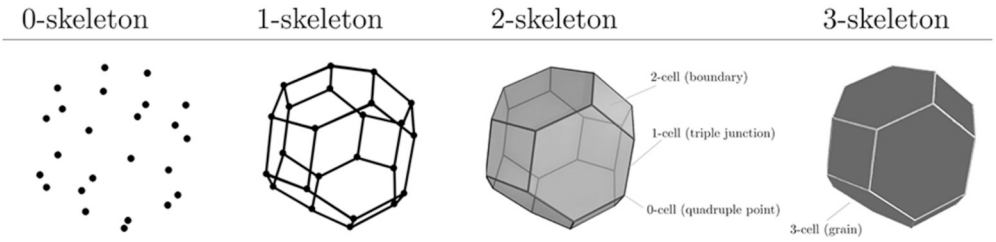

Fig. 2. Illustration of skeletons of a single polyhedron (3-cell). Note, the 3-skeleton of $\mathcal{M}$ is identical with $\mathcal{M}$.

The connectivity of the cells in $\mathcal{T}$ is given by incidence matrices, ∂_k, referred also as the boundary operators, which relate the k-cells to the $(k-1)$-cells on their boundaries for $k \in \{1,2,3\}$. The cells in $\mathcal{T}$ and the incidence matrices form a mathematical structure, $\mathcal{M}$, referred to as 3-complex [36].

A *k-skeleton* of $\mathcal{M}$ is the collection of all m-cells for $0 \le m \le k$. Skeletons of all dimensions are illustrated in Fig. 2, using a single 3-cell. A 2-skeleton is of particular interest in this work as it contains all GBs, TJs, and QPs. The connectivity between the cells of a k-skeleton can be described by adjacency matrices known from the graph and network theories [38,39]. A software library for construction of incidence and adjacency matrices for cell complexes and their skeletons can be downloaded from the web project [40].

Different physical components of a ceramic composite are introduced by assigning identification numbers (IDs) to the cells in $\mathcal{M}$. For example, a simple binary classification of GBs used in [3] leads to identifying all 2-cells as either ordinary (between ceramic grains) or special (containing rGO inclusions). The focus here is on rGO inclusions on GBs, possible cracks along GBs, and potential conglomerations of rGO inclusions on GBs. Thus, four different IDs for 2-cells are used: (i) F_0 for inclusion-free GBs of nanocrystalline ceramic composite; (ii) F_1 for grain boundaries containing single rGO inclusions; (iii) F_2 for cracked grain boundaries (either containing inclusions or inclusion-free; and (iv) F_3 for GBs containing agglomerations of rGO inclusions. The fraction of 2-cells of type F_1 (with rGO inclusions) will be denoted by p, and the fraction of 2-cells of type F_2 (with cracks, with or without inclusions) will be denoted by f. These are given by

$$p = \frac{N_r}{N_2}, \quad f = \frac{N_c}{N_2}, \tag{1}$$

where N_r is the number of 2-cells of type F_1, N_c is the number of 2-cells of type F_2, and N_2 is the total number of 2-cells in the cell complex. A separate notation, p_a, will be used for the fraction of GBs containing agglomerations of rGO inclusions.

2.2. Topological analysis of substructures

The incidence matrices, ∂_k, introduced in Subsection 2.1 provide a practical mathematical tool for topological analysis of cell complexes [3,41]. The k-th combinatorial Laplacian is given by [41]

$$L_k = \partial_k^T \cdot \partial_k + \partial_{k+1} \cdot \partial_{k+1}^T, \tag{2}$$

with two special cases: $L_0 = \partial_1 \cdot \partial_1^T$, and $L_3 = \partial_3^T \cdot \partial_3$. L_k is a positive semi-definite linear operator (square matrix) that maps all k-cells to themselves, collecting local connectivity information. The eigenvalues of L_k are non-negative real numbers, which provide the essential information about the topology formed by the k-cells [42]. The dimension of the nullspace of L_k, i.e., the number of the zero eigenvalues, equals the k-th Betti number, β_k. In particular, β_0 gives the number of connected components of the cell complex, β_1 gives the number of closed loops formed by 1-cells, and β_2 provides the number of closed loops formed by 2-cells, i.e., volumes closed by 2-cells [38].

L_k contains the topological characteristics of the whole k-skeleton, whereas the model of a ceramic composite has 2-cells of different types. The 2-cells of a given type form a substructure which is described by reduced incidence matrices $\widehat{\partial}_k$. The null space of the corresponding reduced Laplacians $\widehat{L_k} = \widehat{\partial}_k^T \cdot \widehat{\partial}_k + \widehat{\partial}_{k+1} \cdot \widehat{\partial}_{k+1}^T$ gives the Betti numbers [43]:

$$\beta_k = \text{Dimension}\left(\text{Nullspace}\left(\widehat{L_k}\right)\right). \tag{3}$$

Taking the substructure formed by 2-cells of type F_2 (cracked GB) as an example, β_0 gives the number of disconnected cracks spanning one or more 2-cells, and β_2 gives the number of 3-cells fully bounded by cracks, i.e., loose material fragments. A derivative topological characteristics is the *inverse connectivity* [44–46]:

$$I_c = \ln\left(\frac{\beta_0}{\beta_2}\right), \tag{4}$$

whose negative values indicate high connectivity in the considered structure.

In-house, open-source codes were used for the construction of cell complexes and substructures: *Polyhedral Cell Complex (PCC) Analyser* [47] (in Python) for construction and analysis of cell complexes from Voronoi tessellations made by Neper [32]; *PCC Processing Design* module [48] (in C++) for assignment of IDs to 2-cells and construction of corresponding substructures; and *Discrete Fracture Kinetic (DFK)* module [49] (in C++) for simulation of intergranular fracture. All modules are freely available from the PRISB project repository on GitHub [50]. The Betti numbers of substructures are calculated by the Processing Design module [48], which uses two additional C++ libraries – Eigen [51] and Spectra [52] to allow for calculating the spectra of large sparse matrices.

2.3. Grain boundary failure

The properties determining the propensity for GB cracking are the cohesive energies of different constituents [30]. The matrix-matrix boundaries of Al_2O_3 can be of two types - 'alpha' and 'gamma' [53]. The experimental estimates for the cohesive energies of these boundaries are 2.6 J/m^2 and 1.6 J/m^2, respectively [54]. As we consider these boundaries to be of one type, F_0, an averaged value of these experimental energies is used as cohesive energy - $\Gamma_m = 2.0$ J/m^2. The measured adhesive energies for rGO-Al_2O_3 interfaces vary between 0.46 J/m^2 and 1.25 J/m^2 depending on the thermal treatments of the composite [55]. An average value is used to represent the cohesive energy of GBs containing a single rGO, i.e., boundaries of type F_1 - $\Gamma_r = 1.0$ J/m^2. The experimental estimate for the surface energy of rGO is 0.18 J/m^2 [24]. Therefore, the cohesive energy of rGO-rGO agglomerates can be estimated to be approximately double the surface energy. The cohesive energy for GBs containing rGO agglomerations, i.e., boundaries of type F_3 is selected to be $\Gamma_a = 0.4$ J/m^2. It is accepted that the boundaries containing agglomerations have a dramatic effect on the composite strength [1].

The fracture energy Σ_{gb} of a GB, i.e., the energy required for cracking, would be equal to the cohesive energy in the absence of other factors. However, it is well-known that stress concentrators, such as

crack tips and agglomerations of inclusions affect significantly the ceramic composite fracture process [4]. This can be viewed as a reduction of the energy required for cracking of a GB by the elastic energy of the local stress concentrators, E_{gb}. Thus, $\Sigma_{gb} = \Gamma_{gb} - E_{gb}$. Failure of a GB occurs when the local stress due to external forces becomes equal to its fracture energy. The effect of external loading is not calculated explicitly. Instead, a simple fracture analysis is performed, whereas at each simulation step the GB with the lowest fracture energy fails first. The fracture process is thus represented as a consecutive formation of nanocracks along GBs, starting with fraction $f = 0$ and continuing until $f \le f_c$, where f_c is a pre-defined critical value of f. Such a simple formulation is sufficient for studies of the fracture network topologies formed at given specific fractions of p and f. We will refer to this model as a kinematic one. The following Subsection 2.4 will address the kinematic approach to structure characterisation allowing to study effect of inclusion patterns on the corresponding IFN topology.

2.4. Elastic energy of stress concentrators

In a PCC created by Voronoi tessellation, each 1-cell (TJ) is a meet of maximum three of 2-cells (GBs), and each 0-cell (QP) is a meet of maximum four 1-cells (TJs) and six 2-cells (GBs) [3,34,56]. A binary classification of 2-cells, e.g., as ordinary and special types, generates four types of 1-cells J_ω, as meets of $\omega \in \{0,1,2,3\}$ special 2-cells [3, 56], and 11 types of 0-cells [31]. Thus, a 1-cell with J_1 is an end of the network of special GBs, a 1-cell with J_2 is an internal TJ in the network of special GBs without local branching, and J_3 is an internal TJ where the network of special GBs branches. In this work, we distinguish between J^r_ω for 1-cells where 2-cells with $\omega \in \{0,1,2,3\}$ rGO inclusions meet, and J^c_ω, for 1-cells where 2-cells with $\omega \in \{0,1,2,3\}$ nanocracks meet.

The effect of stress concentrators is considered by the introduction of structural indices of 2-cells, similarly to the work [3], where they were first associated with stress concentrators around GBs increasing the propensity for cracking. Let α, β, and γ denote the numbers of 1-cells on the boundary of a 2-cell of types J^r_1, J^r_2 and J^r_3, respectively. The GB index characterising the concentration of internal stresses due to inclusions around a single GB is defined as

$$B_L = \alpha + 2\beta + 3\gamma \tag{5}$$

Notably, the GB index B_L can be used to detect the presence of rGO agglomeration in a GB. A simple geometrical consideration suggests that (i) if a GB already contains an rGO inclusion this makes all its TJ of either J_1, J_2 or J_3 type, and (ii) if a GB has more than two TJs of type J_2, it is highly probable that it contains at least two rGO layers. According to Eq. (5), this condition must be satisfied when $B_L \ge 6$. Therefore, it is assumed during the calculations that a GB containing an rGO inclusion contains an agglomeration of inclusions if $B_L > 9$, i.e., if more than 3 adjacent GBs have TJs of type J_3.

Similarly, let μ, λ and γ denote the numbers of 1-cells in the boundary of a 2-cell of types J^c_1, J^c_2 and J^c_3, respectively. The GB index characterising the concentration of internal stresses due to nanocracks around a single GB is defined as

$$C_L = \mu + 2\lambda + 3\gamma, \tag{6}$$

An illustration of GBs with the corresponding GB indices is shown in Fig. 3. These definitions do not account for the variety of GBs geometries, which may range from triangles to polygons with many edges. It is therefore appropriate to normalise them using the number of neighbours of the 2-cell, W_b, which corresponds to the its topological weight introduced in [57]. The normalised indices have values less or equal to 1.

We assume that the elastic energies of the stress concentrators acting locally on GBs, E_{rl} and E_{cl}, depend only on these indices:

$$E_{rl} = \eta_r \cdot \frac{B_L}{W_b}, \tag{7}$$

$$E_{cl} = \eta_c \cdot \frac{C_L}{W_b}, \tag{8}$$

where η_r and η_c are coefficients determining ISC and CSC, respectively. These coefficients are defined using the corresponding cohesive energies as

$$\eta^m_r = C_r\Gamma_m, \ \ \eta^r_r = 0 \tag{9}$$

$$\eta^m_c = C_c\Gamma_m, \ \ \eta^r_c = C_c\Gamma_r, \tag{10}$$

where η^m_r and η^r_r are the η_r values of matrix-matrix (ordinary) GBs and GBs contain rGO inclusion, respectively, and η^m_c and η^r_c are the corresponding η_c values; $\eta^r_r = 0$ due to the assumption that if a GB contains rGO inclusions, the presence of rGO inclusions in the neighbouring GBs does not create further elastic stresses at this boundary.

The coefficients C_r and C_c are greater than 1. If one of these becomes equal to 1, the sum of the corresponding elastic energies of the stress concentrators in a GB, E_{rl} or E_{cl}, becomes equal to the corresponding cohesive energy, Γ_m or Γ_r, leading to GB fracture. A value of C_r or C_c equal to 2 leads to fracture if only half of the neighbouring GBs contain inclusions or cracks. The high stress concentration created by agglomerations of inclusions is not given separate consideration, because they normally fracture first and so effectively act on their neighbours by increasing their C_L indices. To the best of the authors' knowledge, there is no reliable experimental data to date for energies related to stress concentrators in Al_2O_3/rGO ceramic composites. Their values can be very different depending on the particular material, GB size and rGO powder characteristics. As a starting point, we consider $C_r = 1$ and $C_c = 2$. This selection makes cracks in neighbouring GBs twice more "dangerous" than rGO inclusions. It corresponds to qualitative experimental observations of ceramic composite fracture reported in [1]. It will be shown that the CSC to ISC ratio plays a prominent role in the inclusion-mediated process of fracture development, and actually determines the ability to manage crack network topology by the changes in the spatial arrangement of inclusions.

With the introduced elastic energies of stress concentrators, the fracture energy of a GB without inclusions (ordinary matrix-matrix GB) is

$$\Sigma_m = \Gamma_m - E_{rl} - E_{cl}, \tag{11}$$

of a GB with a single rGO inclusion is

$$\Sigma_r = \Gamma_r - E_{cl}, \tag{12}$$

and a GB with agglomeration of inclusions is

$$\Sigma_a = \Gamma_a - E_{cl}. \tag{13}$$

2.5. Configurations of inclusions

The placement of rGO inclusions on 2-cells is either unconstrained, i.e., they are randomly distributed, or subject to a condition that the distribution minimises or maximises the configurational entropy [29, 31,56].

The definition of configurational entropy due to rGO inclusions uses the fractions of TJ types, given by

$$j_i = \frac{N_i}{N_{all}}, \tag{14}$$

where N_i is the number of TJs of type J^r_i, N_{all} is the total number of TJs in the PCC. The configurational entropy due to rGO inclusions is defined by

$$S_{conf} = -(j_0 \cdot log_2 j_0 + j_1 \cdot log_2 j_1 + j_2 \cdot log_2 j_2 + j_3 \cdot log_2 j_3). \tag{15}$$

The entropy is a non-monotonous function of p, with maximum at $p = 0.5$ independent of the material's microstructure [58]. It is an in-

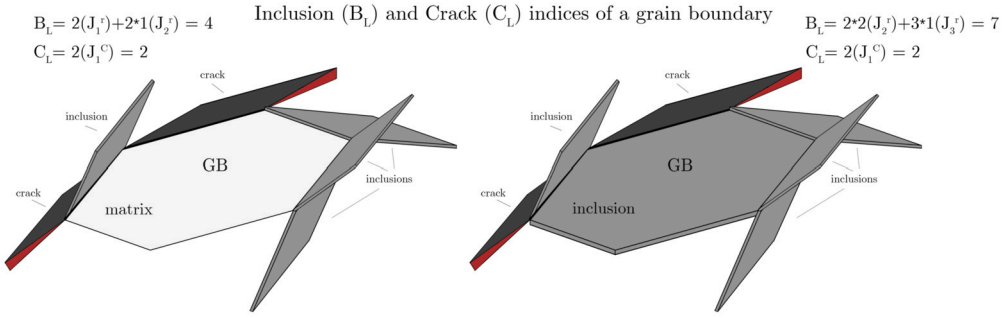

Fig. 3. A sketch of a defect-free grain boundary (left) and a grain boundary containing inclusion (right) with the corresponding values of GB indices B_L and C_L.

tensive microstructure characteristic and its value is independent of the PCC size, providing the size is sufficiently large to represent statistically the microstructure. The entropy corresponds to the Shannon information entropy [56,59], and its value represents the amount of information encoded in the material's defect microstructure. The choice of the logarithm base affects only the units of the configuration entropy; with base 2, S_{conf} expresses the information content in bits [59].

The configurational entropy can have maximum and minimum values for a particular fraction p. These will be denoted by S_{max} and S_{min}, respectively. In addition, S_{rnd} will denote the value of the entropy of randomly distributed inclusions with fraction p.

The configuration with maximum entropy at a given p is realised by assigning special GBs satisfying the principle of maximum entropy production (MEPP) [56,58,60]. To obtain the minimum entropy for a given p, we decompose S_{conf} into two parts [61]:

$$S_{conf} = S_m + S_d, \tag{16}$$

where S_m is a log geometric mean part given by

$$S_m = \frac{1}{4} log_2(j_0 j_1 j_2 j_3), \tag{17}$$

and S_d is a divergence part, describing the deviation of TJs fractions from a homogeneous distribution, given by [61]

$$S_d = \frac{1}{4}\sum_{k<l}(j_k - j_l) log_2\left(\frac{j_k}{j_l}\right) = -\sum_{k=0}^{3}\left(j_k - \frac{1}{4}\right) log_2\left(4 j_k\right). \tag{18}$$

Notably, S_{conf} is maximum when the fractions of TJs of all types are equal. The divergence S_d is negative and measures the distance of a structure from one with maximum configurational entropy. Maximising S_d for a given p, gives the minimum $S_{min}(p)$. This is used to construct a reference configuration with minimum configurational entropy by assigning GBs that maximise S_d.

The random distribution of rGO inclusions provides a benchmark for characterising other specific distributions of special GBs in grain boundary networks (GBN) [3,29,31,62]. The fractions of TJs as functions of fraction p in the random case satisfy the equations [31]:

$$j_0 = (1-p)^3, \quad j_1 = 3p(1-p)^2, \quad j_2 = 3p^2(1-p), \quad j_3 = p^3, \tag{19}$$

where $j_0 + j_1 + j_2 + j_3 = 1$. The entropy of the random distribution can be expressed directly in terms of p by substituting Eq. (19) into Eq. (15) [3].

The three entropies S_{max}, S_{min} and S_{rnd} as functions of the rGO fraction p correspond to three different *reference configurations* resulting from distinct governing principles of rGO spatial arrangement. They are appropriate for characterising other configurations or designs of inclusion networks. The numerical analysis will use them for studies of how these initial configurations affect the induced crack network topology in the same PCC. The PCC Processing Design code [48] has been used to obtain the three rGO configurations.

In addition to the classification of TJs into types J_i, a derivative classification will be used in the calculations and results. Consider only one GB network of a specific type, $F_0, F1$ or, $F2$, the TJs in this substructure can be classified according to the number of incident GBs of the same type. Thus, the "free leafs" have type D_1, branches or loops connected by J_2 junctions have type D_2, and J_3 junctions have type D_3. Let the fractions of TJs of type D_k be denoted by d_k. The fraction d_k^r as a function of p characterises the network of GBs containing rGO inclusions. Similarly, the d_k^c as a function of f characterises the network of cracked GBs. The main difference between the d_k classification and the conventional j_ω classification (see Eqs. (14), is that in the former only specific GBs are considered as if there were no GBs of other types in a PCC. The fractions d_k^r and d_k^c can be calculated directly from the j_ω^r and j_ω^c fractions as

$$d_k^r = \frac{j_k^r}{1 - j_0^r}, \tag{20}$$

and

$$d_k^c = \frac{j_k^c}{1 - j_0^c}. \tag{21}$$

Therefore, at large values of j_0, even small fractions j_ω can give large fractions of the corresponding d_k.

2.6. Mapping mass fraction of rGO powder to fraction of rGO inclusion

The introduced fraction of faces covered with inclusions, p, is a characteristic not measurable directly in experiments. Instead, the mass p_m and volume p_v fractions of rGO powder are widely used. To calculate p corresponding to experimentally measured mass fraction of inclusions p_m, the following relation was proposed [3]:

$$p = p_m d \frac{2\rho}{\kappa \rho_G h_G}, \tag{22}$$

where $\kappa = 83$ is a geometric factor that takes into account sphericity of the Voronoi polyhedrons; ρ_G is the density of rGO, which is close to the density of graphite, i.e., $\rho_G = 2266\ kg/m^3$; ρ is the density of Al_2O_3 ceramics, i.e., $\rho = 3990$ kg/m^3; and h_G is the rGO platelet thickness, assumed to be constant $h_G = 3$ nm (about a dozen atomic layers). The relation between the volume fraction p_v and the mass fraction p_m of inclusions, if required, is given by

$$p_v = p_m \frac{\rho}{\rho_G}. \tag{23}$$

In the calculations, the mass fractions of 1% and 3% of rGO inclusions, achieved experimentally in Al_2O_3 composites [5], are used. These correspond to $p \approx 0.1$ and $p \approx 0.2$, respectively.

3. Results and discussion

Several factors significantly affect a ceramic composite's resistance to cracking. In particular, two factors commonly assumed contributing predominantly to the fracture process: (i) the agglomerations of inclusions with fraction p_a – as the weakest sites where cracks can be easily nucleated (see Eq. (13)), and (ii) the presence of local stress concentrators originated from inclusions and cracks, which were expressed in the developed fracture model by the value of GB indices B_L and C_L (Eqs. (5) and (6)). For addressing materials design tasks, the questions about the significance of both aforementioned factors in their relation to spatial distribution of inclusions and structural characteristics of crack network topology should be resolved. The fraction of rGO inclusions p contributes to both of these factors.

The possibility of managing effectively IFN development by changes in the local ordering (patterning) of inclusions is another key point of our consideration. Polycrystalline ceramic composites technologically often do not allow implementation of any kind of prescribed 3-dimension structure of inclusions, but the creation of random-like patterns deviating from the random case just in their local rGO arrangements is a much more feasible task. Besides the random distribution, two other reference configurations obtained by the maximum (*S-max*) and minimum (*S-min*) configuration entropy production principles will be discussed. They were obtained by the PCC Processing Design code [48] as described previously in Subsection 2.5.

For all the performed simulations, a statistically representative 1000-polyhedron and 3000-polyhedron (see Fig. 1) Laguerre-Voronoi tessellations of a 3-dimensional cube containing more than 12,000 faces and created by Neper software [32] have been used. These tessellations serve us as discrete spaces, replacing conventional continuous manifolds, and can be created just once. All the adjacency, incidence and Laplacian matrices (see Subsection 2.2) of the corresponding PCC were provided by the Voronoi PCC Analyser code [47].

In the current study, the action of external forces is not considered explicitly, which was referred to as a kinematic model. The energies of each GB were calculated by Eqs. (7) - (9) with accounting for stress concentrators effect as it was described in Subsection 2.4. It is assumed that the GBs with lower adhesion energies fracture first, which provides a specific set of GBs for each predefined value of nanocracks fraction f depending on their spatial arrangement (topology) and the fraction p of rGO inclusions in the undamaged material, as discussed in Subsection 2.3.

To provide a comprehensive analysis of the primal rGO and imposed IFN nanocrack microstructures, several tools described in Section 2 have been used: TJ degree distributions d_k, Betti numbers β_i, and the inverse connectivity I_c (see Subsection 2.2) in their dependence on the fractions of inclusions p and cracks f. The following Subsections 3.1 – 3.3 explores the IFN development in the case of the random distribution of rGO inclusions, while the Subsection 3.4 investigates the effects of non-random spatial arrangements of inclusions.

3.1. Fracture network development at the random spatial distribution of rGO inclusions

Let us begin the study with the random spatial distribution of rGO inclusions typical for the composites manufactured in the experimental works, where the use of non-random arrangements of rGO is still rare. The results in this subsection have been obtained for the rGO-Al_2O_3 ceramic composite and the set of adhesion energies ($\Gamma_m = 2.0$ J/m^2, $\Gamma_r = 1.0$ J/m^2, and $\Gamma_a = 0.4$ J/m^2) as described in the methodology Section 2. The value of the coefficient C_c of crack-related stress concentrators (CSC) has been taken equal to $C_c = 2C_r$ – twice larger than the corresponding value of the coefficient C_r of the strength of inclusion-related stress concentrators (ISC).

Let us refer to a GB network *state* any dot in the ternary TJ space with the corresponding values of $d^r = \{d_1^r, d_2^r, d_3^r\}$ or $d^c = \{d_1^c, d_2^c, d_3^c\}$ uniquely representing the degree fractions of nodes of different $k = \{1,2,3\}$ d-types in the rGO inclusion network d_k^r or the IFN of nanocracks d_k^c. Fig. 4a shows two equivalent representations of the d_k^r degree fraction evolution with p at the random spatial distribution of inclusions – three $d_k^r(p)$ plots for $k = \{1,2,3\}$ and the corresponding TJ space containing GB state points with coordinates d^r [44]. In the random case, d_1 degree fractions decrease almost linearly with p, and both the other d_2 and d_3 fractions are relatively small at low fractions of p.

Every initial configuration of inclusions, characterising by the fraction p and the inclusion state vector $\{d_1^r, d_2^r, d_3^r\}$ induces its own topology of the IFN of nanocracks characterising by the fraction f and the state vector of nanocracks $\{d_1^c, d_2^c, d_3^c\}$. As a supporting characteristic, revealing the IFN topology, Betti numbers β_i were calculated in several cases. It is the most resource-intensive part of the calculations required to create Laplacian matrices of a PCC and find their spectra [42] for each value of p and f. Both evolutions of degree fractions (Fig. 5a) and topological characteristics (Fig. 5b) of the IFN in the particular case of $p = 0.2$ randomly distributed rGO inclusions are shown in Fig. 5. Here β_0 shows the number of separate components, which appears to be equal to 1 in the random case; the value β_1 is equal to zero everywhere showing the absence of loops made of nanocracks; and β_2 shows the large numbers of closed areas which are the fragmented parts of the composite. The characteristic of the inverse connectivity $I_c = \ln(\beta_0/\beta_2)$ reveals the growth rate of the crack network connectivity, and the random case possesses a high value of it. The value $\beta_0 = 1$ does mean that at the random spatial distribution of inclusions a whole fraction process develops as a growth of a single fracture component, and there is only one centre of the fracture initiation. It will be shown that it is very different for the other spatial arrangement of inclusions and quite the opposite in the case of the lower CSC.

Ternary nanocrack degree spaces $\{d_1^c, d_2^c, d_3^c\}$ shown on Fig. 6 provides more comprehensive (for several rGO fractions $p = \{0.1, 0.2, 0.3, 0.4\}$) and detailed description of the IFN evolution – changing both with the changes of induced crack fraction f and primal rGO inclusion fraction p. As was discussed in the Introduction section, fracture topology is a key factor influencing the amount of energy dissipated in the material during fracture: long, low-branching cracks (high d_2) are the most dangerous, while the fractal-like structures, possessing a high number of branches (high d_3 value), are optimal in terms of material resistance to fracture.

In the random case, the nanocrack network topology at large fractions of cracked GBs $f \approx 0.3 - 0.4$ remains almost independent on the primal rGO fraction, moving IFN states towards the point $\{0.1, 0.05, 0.85\}$. The scatter of states achieved by the changes of a primal fraction of rGO inclusions p considerably decreases with the increasing of f as the result of fracture process development. Among the interesting features observed in the random case, is that the IFN evolution at $p = 0.1$ is similar to the one that occurred at $p = 0.4$ and possessed an almost constant fraction of $d_2^c \approx 0.05$, but qualitatively different from the cases $p = 0.2$ where the IFN develops almost at constant degree fraction $d_1^c \approx 0.125$.

3.2. Effect of agglomerations of rGO inclusions

By their definition, agglomerations are the GBs containing more than two graphene layers. It is commonly accepted that agglomerations of inclusions contribute to the degradation of a composite's strength. The fraction of GBs containing agglomerations p_a depends equally on the fraction of inclusions p, their geometry (length, aspect ratio, etc.) and spatial arrangement. In the random case, slow growth of p_a starts at $p \approx 0.08$ as it can be seen in Fig. 11b in Subsection 3.4.

To show the effect of agglomerations on the fracture development process, let us effectively remove them from the calculation process simply assuming that GBs containing agglomerations now possess adhesive energies equal to the adhesive energy of all other GBs containing rGO inclusions (1 J/m^2 in Al_2O_3) – making it 2.5 times greater than the

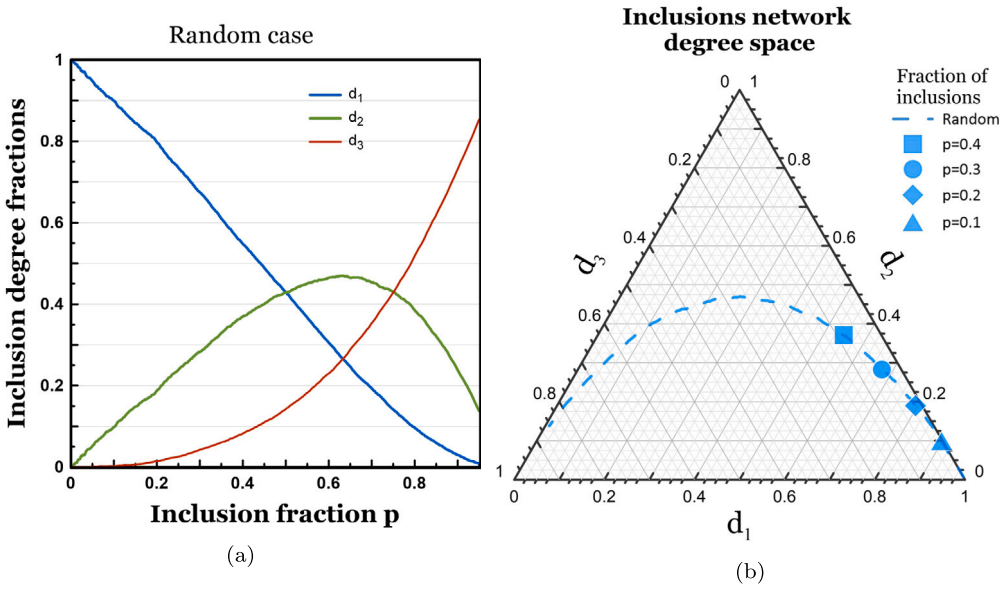

Fig. 4. (a) Inclusions degree distributions d_k^r at their random spatial distribution as the function of rGO fraction p, and (b) another representation of d_k^r as GB state points $\{d_1^r, d_2^r, d_3^r\}$ in the ternary TJ degree space. Here four symbols correspond to the different values of the inclusion fraction $p = \{0.1, 0.2, 0.3, 0.4\}$.

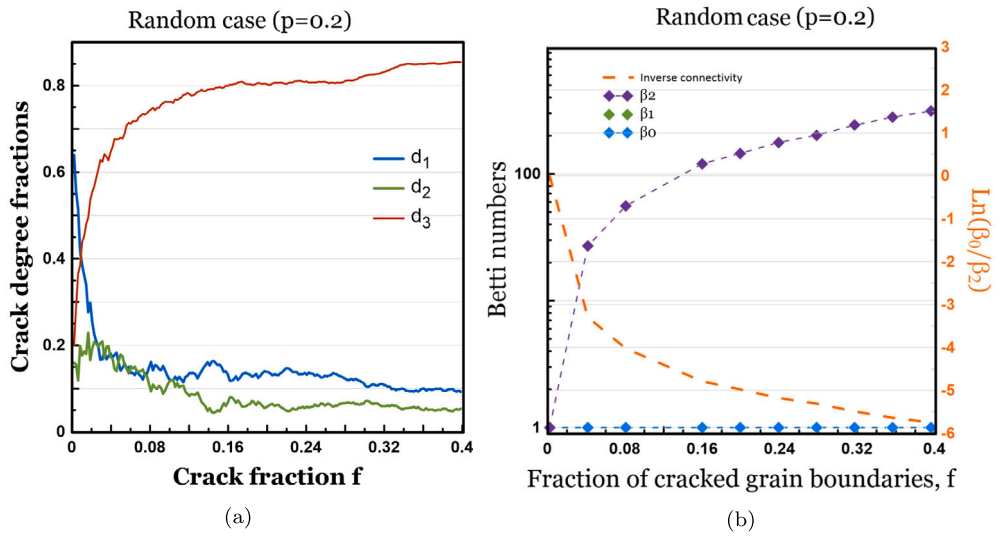

Fig. 5. (a) Evolution of the degree fractions d_k^c of the IFN of nanocracks, and (b) evolution of the topological characteristics β_k and I_c of the same IFN for the random distribution of inclusions with $p = 0.2$. A whole fraction process develops as a growth of a highly connected (low d_1 and d_2) single fracture component ($\beta_0 = 1$).

former agglomeration adhesive energy 0.4 J/m^2. Experimentally, the effect of agglomerations can be mitigated by increasing the adhesive energies between rGO layers by changing their chemical processing and the composite manufacturing technology. Fig. 7 shows the ternary plot for the random case similar to Fig. 6. It can be seen, that the presence of agglomerations does not change the fracture process dramatically. At a large fraction of f, IFN states move to the same fraction d_k^c as before (Fig. 6), but what is important – the absence of agglomeration removes the large scattering of the IFN states, leading to the nearly constant $d_2 \approx 0.07$ fraction, larger clustering of nanocracks (higher d_3 fractions) and correspondingly lower d_1 fractions.

The dashed line shows the boundary of the cropped d_k^c fractions degree space shown previously in Fig. 6.

3.3. Effect of stress concentrators in triple junctions of grain boundaries

Stress concentrators of inclusions are another significant factor commonly referred to in fracture mechanics. Such concentrators serve as sites for early crack nucleation dramatically decreasing materials' persistence to fracture. In our discrete model, it is assumed that the presence of inclusions in the neighbours of a ceramic GB interacts with it throughout their common TJs. Clustering of rGO inclusions not only creates local spatial inhomogeneity but also greatly increases the value of the local GB index B_L (Eq. (5)), provoking clustering of nanocracks in the GB surroundings. In their turn, cracks also create local stress concentrators in the neighbouring GBs (see Fig. 3), and during the cracking process a value of the corresponding index C_L growth significantly (Eq. (6)). Fig. 8 demonstrate B_L (Fig. 8a) and C_L (Fig. 8b) GB indices in the random case of spatial distribution of inclusions for two moderate values of $p = 0.1$ and $p = 0.2$. Despite the fewer number of GBs possessing large C_L indices, compared to the B_L distribution, a substantial amount of GBs with very high values of the C_L index are clearly seen.

If the effect of the stress concentrators related to the crack index C_L significantly overcomes the effect of the inclusion index B_L, then the fracture process becomes governed solely by the IFN development and

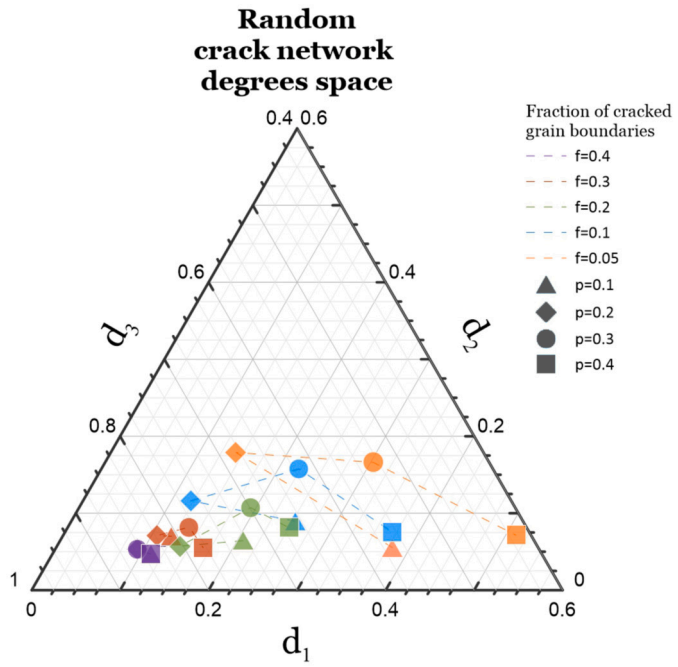

Fig. 6. d_k^c fractions degree space at the random spatial distribution of rGO inclusions. Each dotted line and colour represents changes in the IFN topology with an increase in the fraction of fractured GBs $f = [0.05, 0.4]$ at a given initial fraction of rGO inclusions $p = [0.1, 0.4]$.

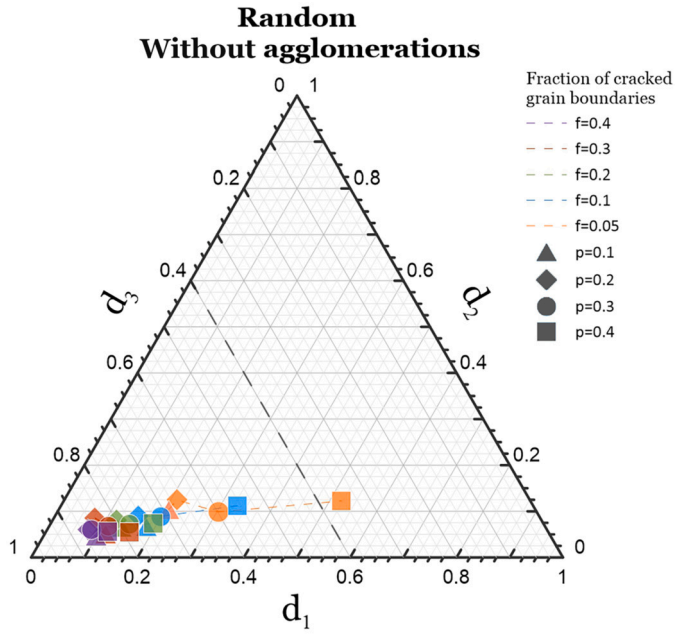

Fig. 7. d_k^c fractions degree space at the random spatial distribution of rGO inclusions in the absence of their agglomerations. Each dotted line and colour represents changes in the IFN topology with an increase in the fraction of fractured GBs $f = [0.05, 0.4]$ at a given initial fraction of rGO inclusions $p = [0.1, 0.4]$.

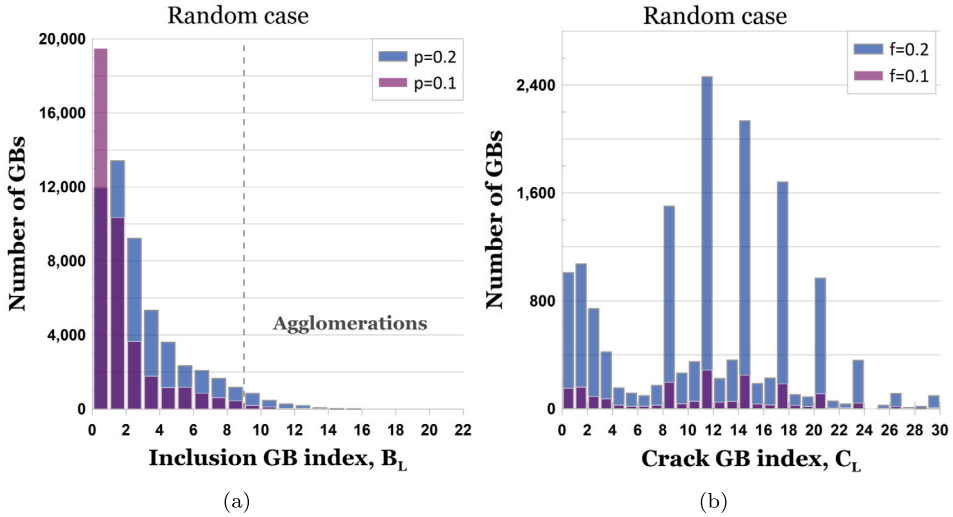

Fig. 8. (a) B_L and (b) C_L GB index distributions at the random distribution and two moderate values of inclusions $p = 0.1$ (purple) and $p = 0.2$ (blue). Large values of the B_L index to the right of the dotted line are associated with the presence of rGO agglomerations.

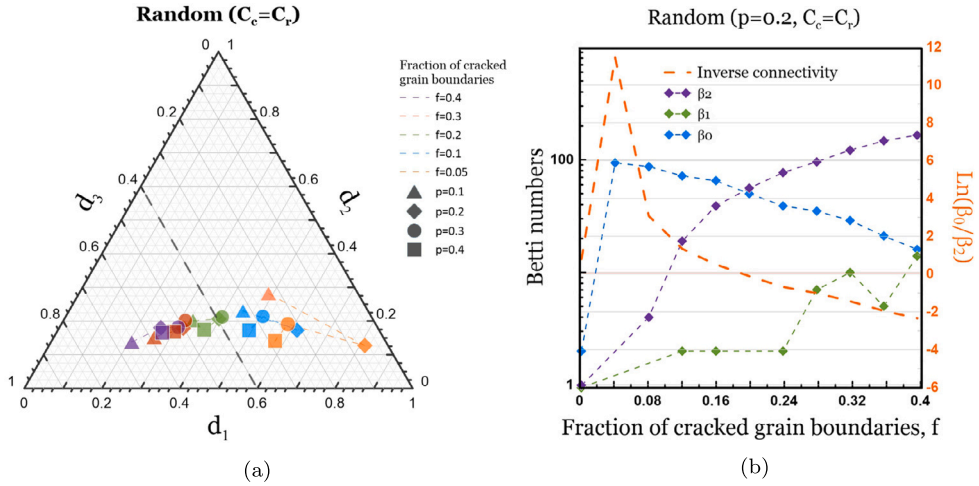

Fig. 9. (a) d_k^c fractions degree space and (b) evolution of the topological characteristics β_k and I_c of the same IFN with $p = 0.2$ at the random spatial distribution of rGO inclusions and twice lower elastic stress concentrators related to nanocracks $C_c = C_r$ (see Eq. (9)). Here β_0 represents the number of separate components in the IFN, while β_3 values are associated with the number of volumetric fragments. Negative values of $I_c < 0$ indicate high IFN connectivity.

inclusions can just slightly mediate it, as it was revealed in the previous simulation results (Figs. 6 and 7).

To date, a few works demonstrate the local energy value related to graphene inclusion [4], but still, there are no estimations for local elastic energies created by the presence of rGO inclusions and their agglomerations in the neighbouring GBs. Moreover, the thickness of rGO inclusions can vary widely [63], changing the ratio C_c/C_r of the stress concentrators related to inclusions and cracks (see Eq. (9)). It was initially taken as $C_c/C_r = 2$, but in the experiment, this ratio depends on numerous factors, including the particular dimensions of inclusions and nanocracks. The simulations below (Fig. 9) demonstrate the effect of decreasing twice the power of the stress concentrators related to nanocracks by taking the ratio $C_c/C_r = 1$ in Eq. (9). The dashed line shows the boundary of the cropped ternary TJ space shown previously in Fig. 6.

Opposite to the previous case of the elimination of the rGO agglomerations effect, the C_c/C_r ratio affects the IFN topologies entirely, twice widening the scatter of the achievable d_1 values. An average value of d_2 is also twice larger than it was in the cases considered previously. At large fractions of cracked GBs, $f \approx 0.3 - 0.4$, the TJ degree states are accumulating around the point $\{0.3, 0.15, 0.55\}$. Fig. 9b shows the behaviour qualitatively different from Fig. 5b. The IFN here demonstrates about a hundred separate components β_0, that suggest multiple independent origins of the IFN growth, maintaining the network connectivity relatively low. The number of loops β_1 grows gradually. All these factors signify the importance of the ratio of local elastic energies between the different sources of stress concentrators.

The following Subsection 3.4 discusses the significance of spatial rGO rearrangements for the IFN topology.

3.4. *Effect of spatial arrangement of rGO inclusions*

This subsection addresses the most significant question of how the various local patterns of the primal structure of rGO inclusions and the corresponding changes in the rGO network characteristics may cause different IFN topologies. In other words, one shall study how changes in the primal spatial arrangement of rGO inclusions can modify the ultimate cracking behaviour of the considered Al_2O_3 composites making it manageable. Let us use two reference rGO configurations corresponding

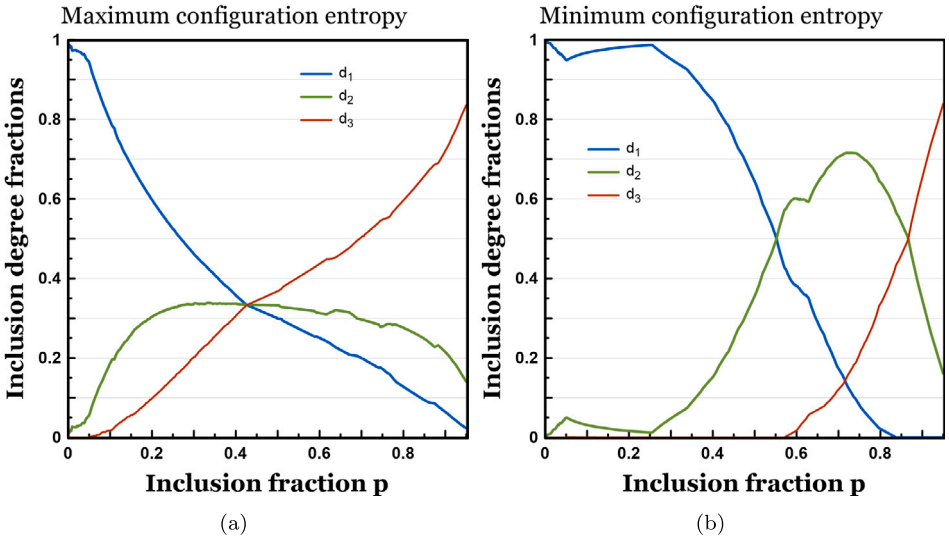

Fig. 10. Inclusions degree distributions d_k^r at the two considered reference configurations of inclusions: (a) maximum configuration entropy (S-max), and (b) minimum configuration entropy (S-min).

to the minimum configuration entropy (S-min) and the maximum configuration entropy (S-max) cases discussed in Section 2.5. Both these configurations are qualitatively different from the random case and each other, but no one of them is a quasi-regular structure and all their differences are only in the local rGO patterning.

Let us first study the initial case with the set of parameters described in Section 2, including the low agglomeration energy $\Gamma_a = 0.4$ J/m^2 and the inclusion to crack stress concentrators ratio $C_c/C_r = 2$. Fig. 10 shows the changes of the d_k^r inclusion degree fractions with p for the considered S-max (Fig. 10a) and S-min (Fig. 10b) cases. These figures should be compared with the similar Fig. 4a corresponding to the random case. In the S-max case, D_2 types of TJs give the corresponding degree fraction $d_2^r > 0.2$ already at $p \approx 0.1$ and after $p = 0.2$ it roughly maintained almost a constant value of $d_2^r \approx 0.3$. The fraction of D_3 type junctions grows almost linearly starting at $p \approx 0.05$ in this case achieving $d_3^r \approx 0.3$ already at $p = 0.4$. For comparison, the same value of D_3 TJ fraction is achieved at $p \approx 0.65$ in the random case and $p \approx 0.8$ in the S-min case. The S-min case naturally maximises the homogeneity of the TJ system: before $p \approx 0.4$ it generates mostly D_1 junctions, after that maximising D_2, and finally, after $p \approx 0.8$, it grows D_3 fraction which maintained almost zero before $p \approx 0.6$.

Fig. 11a shows differences in the topology of the rGO network in all the three considered reference configurations. In addition, Fig. 11b demonstrate significant differences in the fractions of agglomerations p_a as the function of inclusion fraction p. The S-max case possessed a considerable fraction of agglomerations even at a relatively small fraction of inclusions demonstrating linear growth starting from 5% of inclusions. In the opposite S-min case, agglomerations are almost absent before the fractions of inclusions $p \approx 0.32$. Fig. 12 provides a more detailed picture of the local agglomeration of inclusions expressed as B_L index distribution for the considered S-max and S-min reference configurations and two moderate values of $p = 0.1$ and $p = 0.2$. The most interesting feature here is the bimodal distributions of the B_L index at the S-max configuration of inclusions, leading to the large fractions of agglomerations and rGO-related stress concentrators. This figure is similar to Fig. 8a for the random case, where the distribution is apparently unimodal.

IFN development in the S-max and S-min references configurations at the initial fraction of inclusions $p = 0.2$ is shown in Fig. 13 and Fig. 14. In comparison with the analogous Fig. 5 it shows much larger fractions of d_1^c and d_2^c TJ d-types with $\beta_0 \approx 8 - 10$, suggesting a forest-like structure development instead of a single tree-like component observed in the random case.

In the S-max and S-min cases, IFN develops as the simultaneous growth of several components. The characteristics of the inverse connectivity $\ln(\beta_0/\beta_2)$ show that the maximal connectivity in the fracture network at $f = 0.4$ is achieved in the random case, while minimal at the S-min case. At the same time, the S-max case possesses the highest connectivity increase rate. It is interesting to note that in the S-max (at 6% fraction of cracks) and S-min (at 4% fraction of cracks) cases of the rGO spatial distribution the value of the inverse connectivity of the IFN cross zero value, that can be interpreted as a kind of topological phase transition [44].

Fig. 15 shows the ternary representation of the IFN topology at a few different fractions $p = \{0.1, 0.2, 0.3, 0.4\}$ of rGO inclusions in the considered S-max and S-min cases of their spatial distribution. For clarity, the whole degree space is cropped here similarly to Fig. 6. In the S-min case, likewise the random case (see Fig. 6), the IFN topology at large fractions of cracked GBs $f \approx 0.4$ remains almost independent on the rGO fraction and spatial distribution of inclusions moves towards the TJ fraction degree state $d^c = \{0.1, 0.05, 0.85\}$. The S-min case is also clearly characterised by a nearly constant degree fraction $d_2^c \in [0.05, 0.1]$. At the S-max spatial distribution of inclusions, the fraction degree state moves towards another point $d^c = \{0.175, 0.1, 0.725\}$ with a twice higher fraction of D_2 junctions.

Analysis reveals that at a high value of the stress concentrators $C_c \gg C_r$ related to nanocracks it is hardly possible to increase significantly d_1^c or d_2^c fractions through the changes in spatial arrangement of rGO inclusions. The effect of the spatial rearrangement of rGO becomes considerable only for the small fraction of cracked GBs $f \sim 0.05 - 0.1$.

As it has been shown for the random spatial distribution of inclusions, the decrease in the CSC to ISC ratio provides the most efficient tool of management IFN topology. Fig. 16 shows the distribution of the number of GBs possessing the specific values of C_L index in the IFN. In the both considered S-max and S-min cases high peaks are seen in the area of low C_L values contrasting with the random case distributions shown in Fig. 8b.

In Fig. 17 shown TJ degree spaces of the IFN corresponding to the S-max and S-min rGO spatial distributions possessed twice lower CSC to ISC ratio $C_c/C_r = 1$. The dashed line shows the boundary of the cropped ternary TJ spaces shown previously in Fig. 6 and Fig. 15. In this case, as initial stages of the IFN development with $f \approx 0.05 - 0.1$, as the late

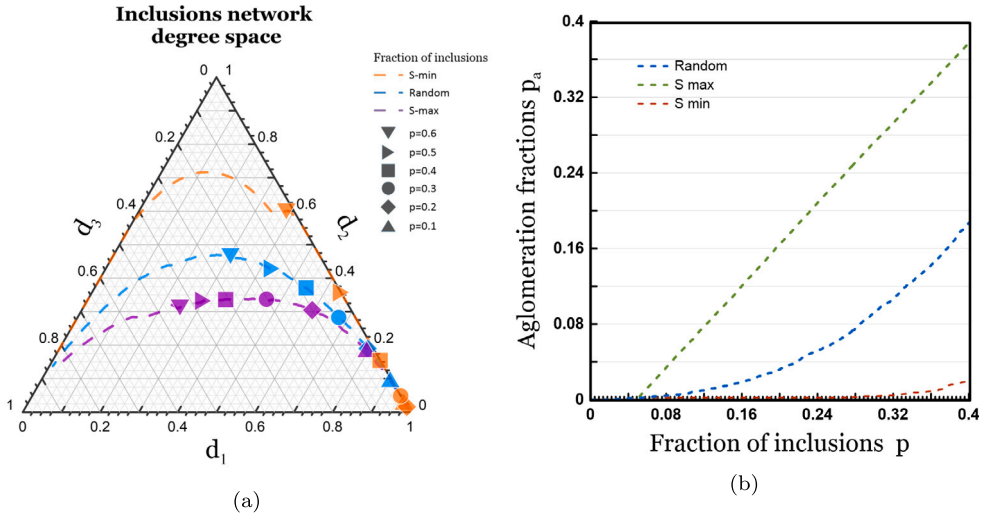

Fig. 11. (a) Ternary TJ degree space of inclusions, and (b) agglomeration fractions p_a as the functions of inclusion fraction p in all the three considered reference configurations.

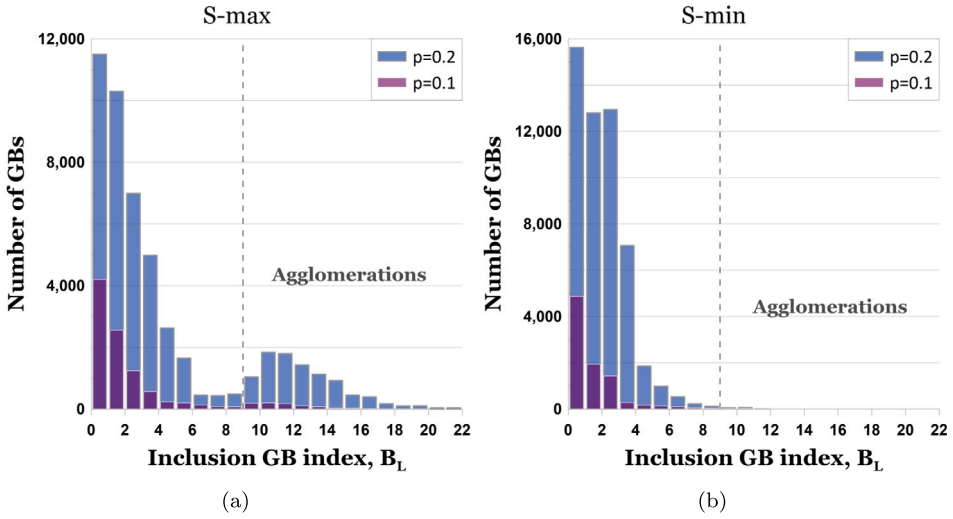

Fig. 12. B_L index distributions for the S-max and S-min considered reference configurations at two moderate fractions of inclusions $p = 0.1$ (purple) and $p = 0.2$ (blue). Large values of the index to the right of the dotted line are associated with the presence of rGO agglomerations.

stages with $f \approx 0.3 - 0.4$ can be effectively managed by changes in the rGO fraction p and their local patterning.

It looks especially promising that in the S-max case at $p \approx 0.2$ the state $d_c^r = \{0.3, 0.2, 0.5\}$ can be achieved at $f = 0.4$. The IFN contains nearly 3 times larger d_1^c and d_2^c fractions compared to the random case at the ratio $C_c/C_r = 2$ (providing $d_c = \{0.1, 0.05, 0.85\}$) that indicates the maintaining of the forest-like IFN structure with multiple independently growing components even at large fractions of f.

Similar effects can be explicitly visible in the 2D case of structure evolution corresponding to a thin film cracking process. While it is not similar to the considered 3D case, the 2D fracture process provides visually comprehensible pictures of the IFN development process and clearly demonstrates the effect of the CSC to ISC ratio. All the simulations presented in Appendix A have been performed with the same kinematic fracture model which was used in the 3D case. The PCC has been replaced with the 2D Voronoi tessellation of a plane containing 5,000 polytopes corresponding to Al_2O3 ceramic grains. In the 2D case, edges correspond to GBs and nodes to TJs.

4. Discussion and conclusions

Most of the studies in the design of ceramic polycrystalline composites, including nanocomposites, still operate only with mass fractions of different types of inclusions distributed randomly or quasi-randomly in the matrix. This approach cannot provide the desired flexibility in controlling the mechanical and physical characteristics of the composites. Special spatial ordering of inclusions should extend significantly the range of achievable mechanical properties, but the specific requirements for such ordering as well as its effect on the development of fracture network remains unclear. Several recent studies highlight the primal importance of the spatial distribution of rGO plates [3,64,65] and their geometry [66]. Additive and powder-based manufacturing allow high flexibility in tailoring the internal architecture of the rGO inclusion network [20,67]. Although the manufacturing of prescribed highly-ordered inclusions' networks [1] incorporated into ceramic matrix still looks unrealistic, the creation of specific local ordering of inclusions is a much more feasible task. For instance, changing the geometry and length distribution of inclusions in rGO powder is one of the options

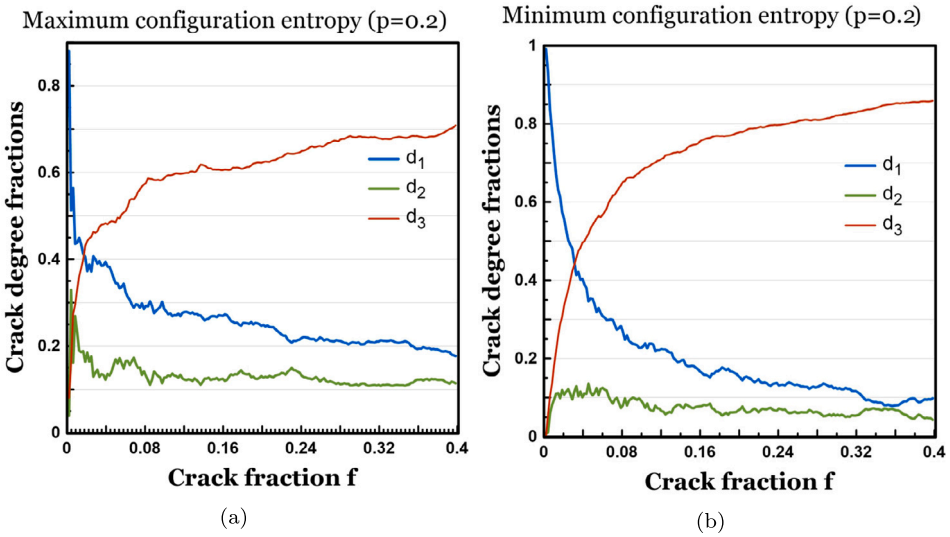

Fig. 13. Evolution of the TJ degree fractions d_k^c in the IFN of nanocracks developed at the initial fraction of inclusions $p = 0.2$ at (a) S-max and (b) S-min configurations of inclusions.

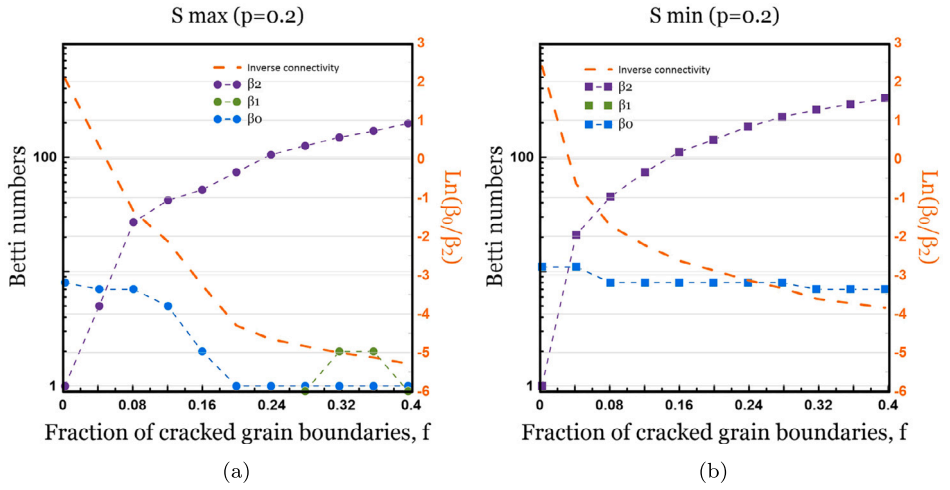

Fig. 14. Evolution of the topological characteristics β_k and I_c for the (a) S-max and (b) S-min distributions of rGO inclusions with fraction $p = 0.2$. Here β_0 represents the number of separate components in the IFN, while β_3 values are associated with the number of volumetric fragments. Negative values of $I_c < 0$ indicate high IFN connectivity.

for easy practical implementation of such local ordering. As it has been stated in [66]: "graphene with low thickness and large lateral size was more beneficial to improve mechanical properties of ceramic composites". The possible drawback of such ordering is the nonlinear growth in the average number of agglomerations of inclusions and the associated growth of local stress concentrators. Studied ceramic nanocomposites, like Al_2O_3 based nanoceramics, with reduced graphene oxide (rGO) inclusions combine the advantages of a hard ceramic matrix and soft graphene inclusions serving as an excellent electrical conductor and providing several toughening mechanisms, such as bridging, crack deflection and branching [4,21]. The main barrier to advances in this design area is the restrictions of continuous approach in characterising the primal rGO inclusion network and the induced fracture network (IFN) topology. It makes "trial and error" the leading approach, which is not economic and practical for developing a new generation of ceramic-graphene nanocomposites with properties dependent on the graphene network configuration.

A new state-of-the-art fully discrete methodology developed in this study naturally overcomes such difficulties allowing for prediction of the topology of the nanocrack network emerging in the composite at three principally different reference configurations of rGO inclusions: random spatial distribution, and distributions characterised by maximal and minimal diversity in local rGO-rGO junctions. A topologically realistic model of the ceramic-graphene nanocomposite based on the 3-dimension Voronoi tessellation of space allowed for investigating the effects of rGO agglomerations in grain boundaries alongside the action of the rGO-related (ISC) and nanocrack-related (CSC) stress concentrators. The experimental data about the adhesion energies of rGO-rGO, rGO-matrix and matrix-matrix grain boundaries in Al_2O_3 ceramic and the calculated spatial arrangement of ISC and CSC were used to determine the specific set of fractured grain boundaries and characterise the topological states of their network. Agglomerations serve as weak spots with several times lower adhesion energy compared to all other GBs. The developed PCC Processing Design [48] software tools made it possible to design numerically special inclusion ordering to control the structures of multiple cracking in nanoceramic composites and revealed the most significant factors that affected the induced topology of the IFN.

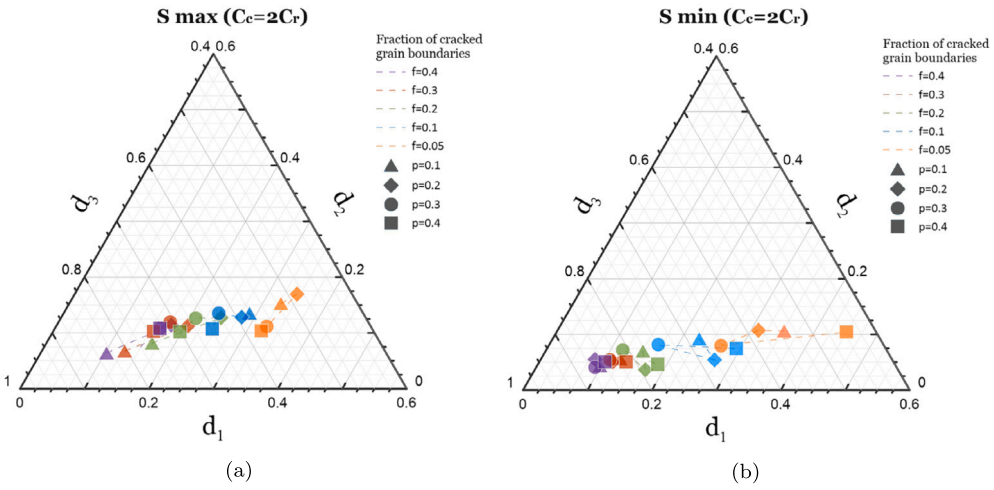

Fig. 15. d_k^c TJ fractions degree space at the (a) S-max and (b) S-min spatial distributions of rGO inclusions. Each dotted line and colour represents changes in the IFN topology with an increase in the fraction of fractured GBs $f = [0.05, 0.4]$ at a given initial fraction of rGO inclusions $p = [0.1, 0.4]$.

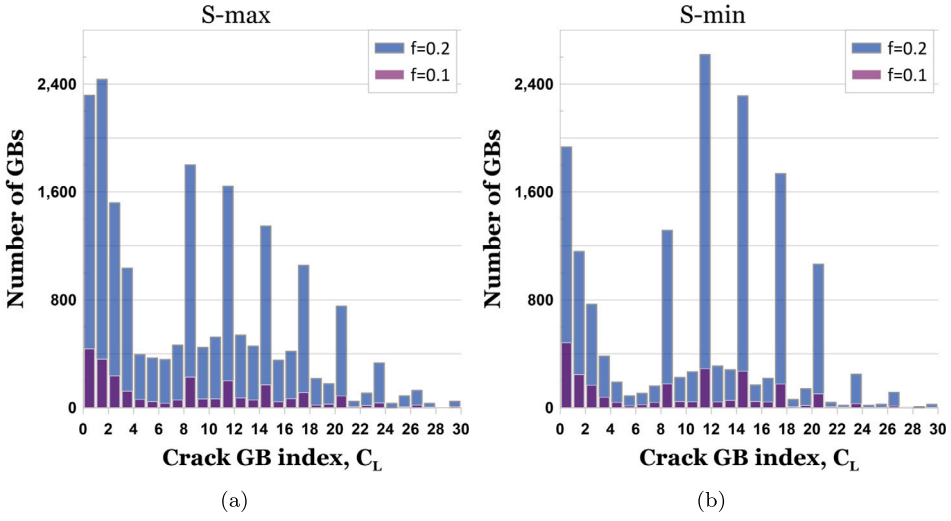

Fig. 16. C_L index distributions for the S-max and S-min reference configurations at two moderate fractions of inclusions $p = 0.1$ (purple) and $p = 0.2$ (blue).

Simulations were performed for a wide range of primal fractions of rGO inclusion – from 1% to a few mass per cent of rGO demonstrating the evolution of the IFN topology up to the fractions of nanocracks (associated with damage value) equal to 40% of fractured GBs. It has been demonstrated that an increase in the fraction of rGO inclusions has a significant effect on the IFN at the early stages of the fracture process (below ≈1 mass per cent) and, what is more surprising, the IFN structure can be topologically close at twice larger rGO fraction, while its moderate increase can abruptly cause very different topological states. At any stage of the IFN development, the increase of the rGO fraction above 2% mass per cent becomes low effective for the modification of IFN topology and at the same time should affect negatively the strength of the composite. On the contrary, the local ordering of rGO inclusions can significantly affect the IFN development at any stage of its development but its effect is massively determined by the ratio of the local stress concentrators related to inclusions (ISC) and nanocracks (CSC). This ratio appears to be the most significant factor affecting the IFN topology: the nanocrack network develops as a single highly connected component at high CSC/ISC ratios much greater than 1 and as a "forest" containing several independently developing components at its low ratios tend to 1. Hence, only the composites with low CSC/ISC ratio allow to use effectively rGO spatial redistribution to govern the whole IFN development, so that the local ordering of rGO inclusions can provide an effective control tool for tailoring IFN topology. In practice, this ratio should depend strongly on the grain size distribution of the nanocomposite determining the average size and the related elastic energy of nanocracks, and the rGO thickness distribution which can be practically varied in a wide range – from one graphene layer to the flakes about micrometre in size.

The agglomerations of inclusions play an equivocal role in the IFN development: they increase the number of weak points for fracture nucleation, negatively affecting the composite's strength, but, at the same time, increase spatial homogeneity of the IFN and so the amount of total dissipated energy during the fracture process. The agglomeration effect is quite notable even in the random case of rGO spatial distribution. The scattering of the achievable topological states of the IFN significantly decreases with the increasing of rGO inclusions' fraction and decreases the number of rGO agglomerations. In that sense, a reasonable increase in the amount of agglomeration can be a positive factor.

At any performed modifications of the initial rGO inclusions topology it was not possible to achieve the nanocrack network with the fraction of the d_2 type junctions corresponding to the elongated chains of

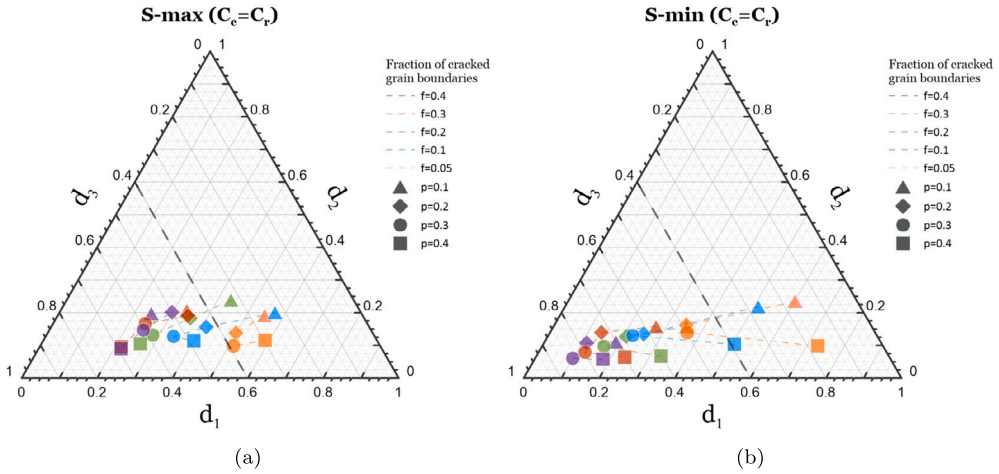

Fig. 17. d_k^c TJ fractions degree space at the (a) S-max and (b) S-min spatial distribution of rGO inclusions at low value of stress concentrators $C_c = C_r$ related to nanocracks. Each dotted line and colour represents changes in the IFN topology with an increase in the fraction of fractured GBs $f = [0.05, 0.4]$ at a given initial fraction of rGO inclusions $p = [0.1, 0.4]$.

nanocracks exceeded 30%. In most simulation cases, highly fragmented tree-like structures with a high value of d_1 type junctions ("leaves") are observed at low fractions of fractured GBs moving towards a cell structure possessing a high value of d_3 type junctions at high fraction of nanocracks.

As a rule of thumb, the rGO plates with the thickness of a few graphene layers, whose elastic fields are comparable to the corresponding fields of the surrounding nanocracks and a reasonable amount of rGO agglomerations for increasing large-scale stress homogeneity can be generally suggested. More accurate inclusion network design can be effectively computed at each particular practical case using the developed methodology and software tools [48,50].

Several other valuable aspects can be considered in further works: the effect of the size distribution of rGO inclusions, the electrical conductivity of their network, more types of grain boundaries, the inclusion of α and γ types of ceramic matrix boundaries and different types of graphene-like inclusions. Novel experimental methodologies like X-ray tomography [68] and 3D EBSD analysis open exciting perspectives for the characterisation of rGO spatial distributions and the development of fracture networks. Recent developments in additive manufacturing [20] make possible management of defect microstructures on the microscale level. On the other side, the common case of the macroscopic crack growth accompanied by the pre-fracture events in their processing zones and the effect of the complex stress state can be considered straightforwardly using the developed methodology and programming tools. Our ongoing task is to supplement the developed purely kinematic model with the explicit consideration of external stresses and macroscopic cracks growth providing a more comprehensive picture of the composite's fracture development both on the microscopic and macroscopic levels. All the outcomes of the present paper remain correct in such a multi-scale consideration to describe the local development of the IFN topology in the vicinity of macrocracks and suggest an optimal ratio between CSC and ISC.

CRediT authorship contribution statement

E.N. Borodin: Conceptualization, Formal analysis, Methodology, Software, Visualization, Writing – original draft, Writing – review & editing. **A.G. Sheinerman:** Methodology, Writing – review & editing. **O.Yu. Bushuev:** Data curation, Software, Writing – review & editing. **M.Yu. Gutkin:** Funding acquisition, Methodology, Project administration, Writing – review & editing. **A.P. Jivkov:** Conceptualization, Funding acquisition, Methodology, Writing – review & editing.

Declaration of competing interest

The authors declare that they have no known competing financial interests or personal relationships that could have appeared to influence the work reported in this paper.

Data availability

Data will be made available on request.

Acknowledgements

Borodin and Bushuev acknowledges the support of the Engineering and Physical Sciences Research Council (EPSRC) UK, via grant EP/V022687/1 (PRISB), for the support in development of the PCC Processing Design software. The studies of ceramic-graphene nanocomposites have been supported by the Russian Science Foundation through the grant No. 18-19-00255, https://rscf.ru/project/18-19-00255/. Jivkov acknowledges the support of EPSRC UK, via grant EP/N026136/1 (GEMS), for development of approaches to analysis on discrete complexes in solid mechanics.

The authors confirm that the data supporting the findings of this study is available within the article. Some of the raw/processed data required to reproduce these findings can be found on the http://materia.team project webpage.

Appendix A. 2D simulations of the IFN development

Figures below show several 2D sketches representing IFN development in the same 2D cut of a PCC in two reference cases (Subsection 2.5) corresponding to the random generation of inclusions and their arrangement corresponding to the maximum configuration entropy (S-max) at two different CSC to ISC ratios.

In the random case of the rGO primal distribution and the high ratio CSC/ISC = 2 (Fig. A.18).

In the random case of rGO primal distribution and the low ratio CSC/ISC = 1 (Fig. A.19).

In the S-max case of rGO primal distribution and the high ratio CSC/ISC = 2 (Fig. A.20).

In the S-max case of rGO primal distribution and the low ratio CSC/ISC = 1 (Fig. A.21).

Typical rGO and IFN local patterns at S-max reference configuration high and low CSC to ISC ratio are shown in Fig. A.22.

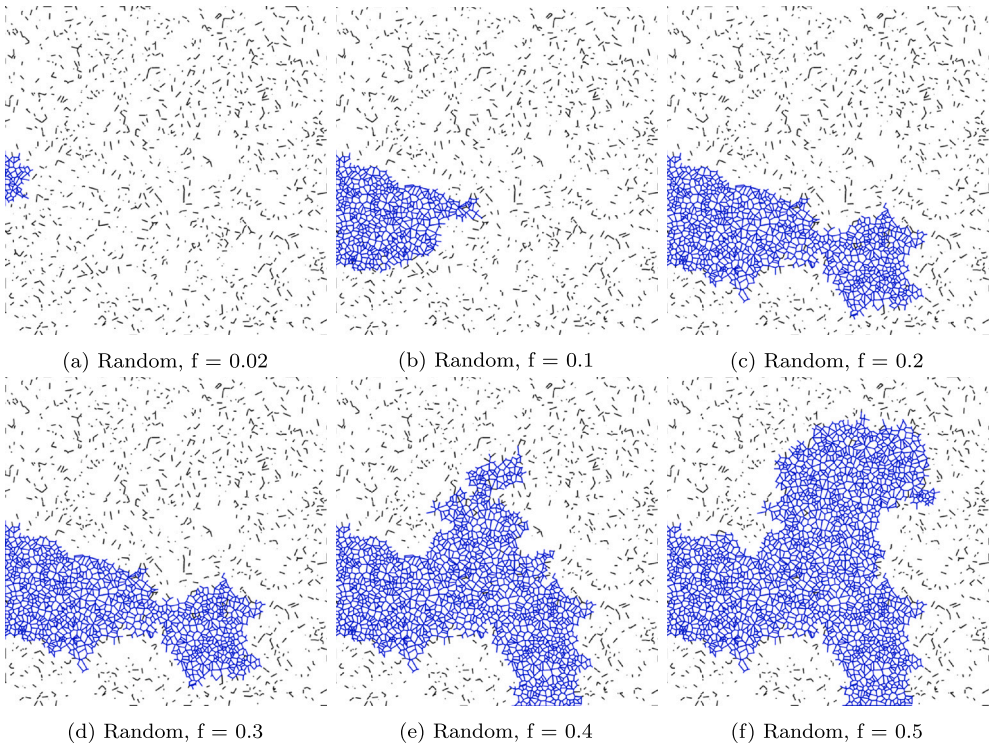

Fig. A.18. 2D visualisation of microstructures of the random distribution of rGO inclusions (black) and IFN of nanocracks (blue) with their typical patterns at $p = 0.1$, high ratio CSC/ISC = 2 and (a) $f = 0.02$, (b) $f = 0.1$, (b) $f = 0.2$, (b) $f = 0.3$, (b) $f = 0.4$, (b) $f = 0.5$.

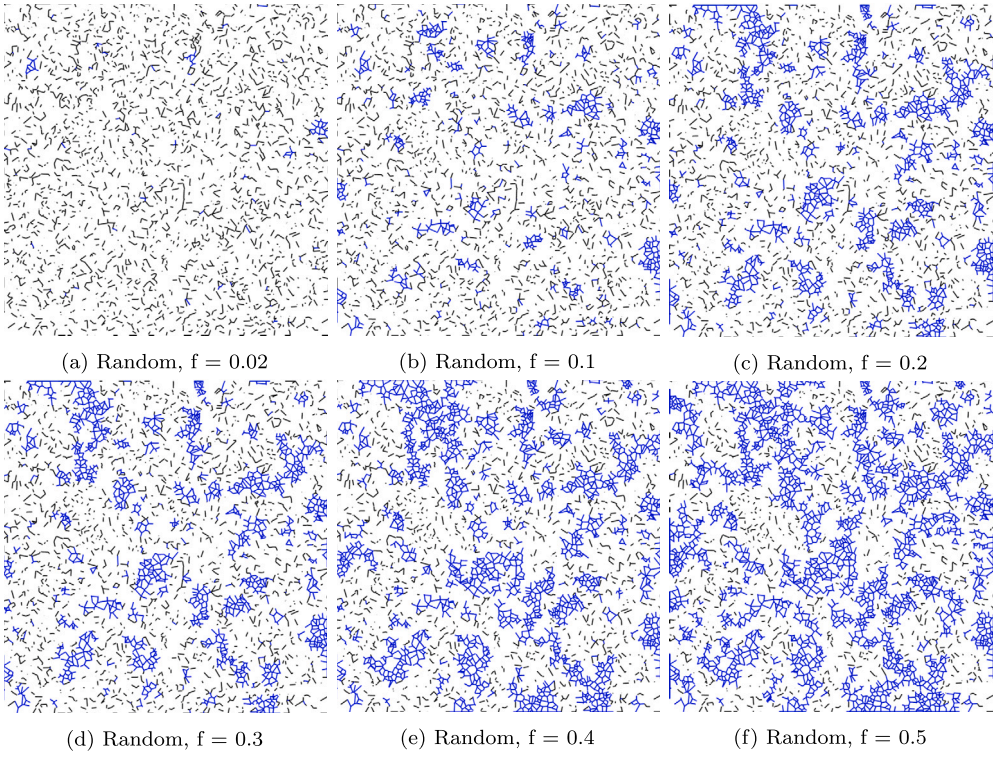

Fig. A.19. 2D visualisation of microstructures of the random distribution of rGO inclusions (black) and IFN of nanocracks (blue) with their typical patterns at $p = 0.2$, low ratio CSC/ISC = 1 and (a) $f = 0.02$, (b) $f = 0.1$, (b) $f = 0.2$, (b) $f = 0.3$, (b) $f = 0.4$, (b) $f = 0.5$.

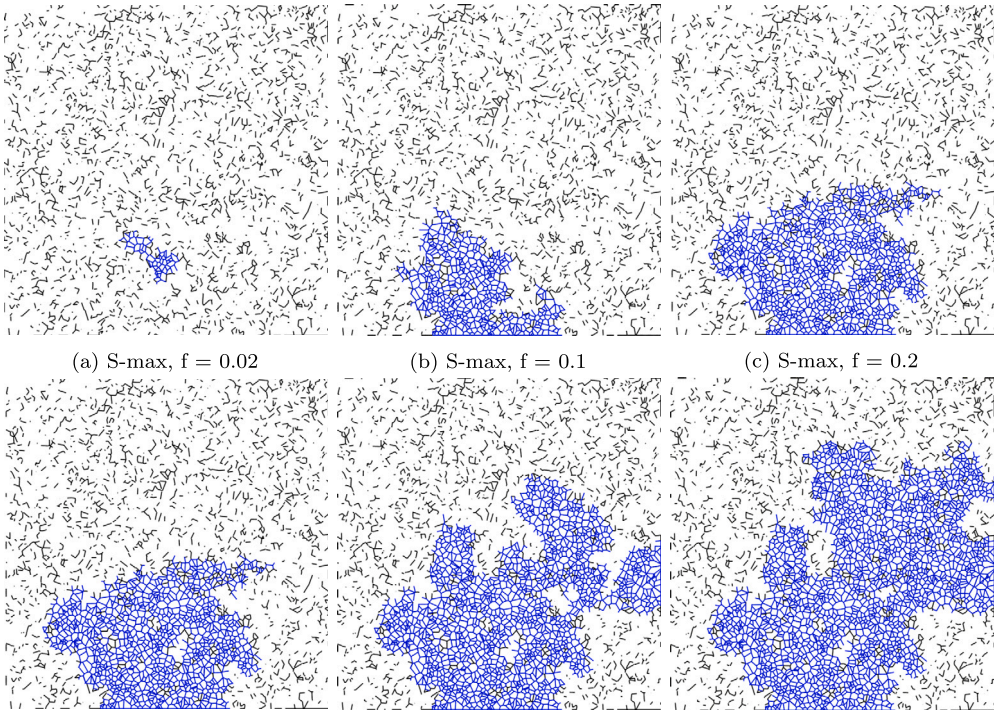

Fig. A.20. 2D visualisation of microstructures of the S-max distribution of rGO inclusions (black) and IFN of nanocracks (blue) with their typical patterns at $p = 0.1$, high ratio CSC/ISC = 2 and (a) $f = 0.02$, (b) $f = 0.1$, (b) $f = 0.2$, (b) $f = 0.3$, (b) $f = 0.4$, (b) $f = 0.5$.

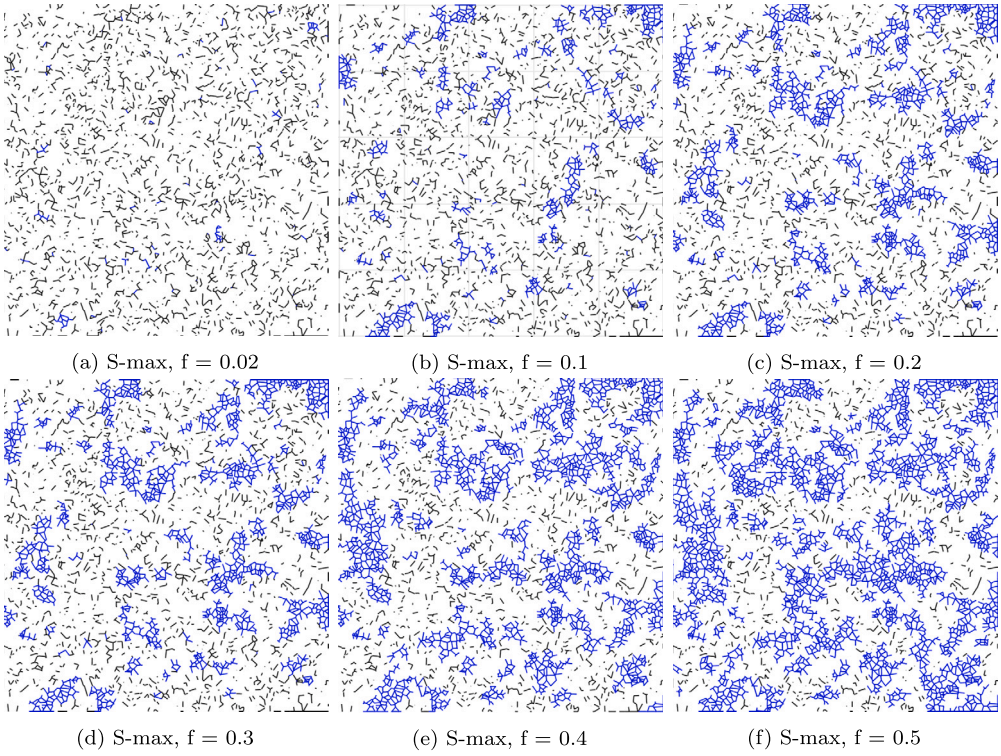

Fig. A.21. 2D visualisation of microstructures of the S-max distribution of rGO inclusions (black) and IFN of nanocracks (blue) with their typical patterns at $p = 0.2$, low ratio CSC/ISC = 1 and (a) $f = 0.02$, (b) $f = 0.1$, (b) $f = 0.2$, (b) $f = 0.3$, (b) $f = 0.4$, (b) $f = 0.5$.

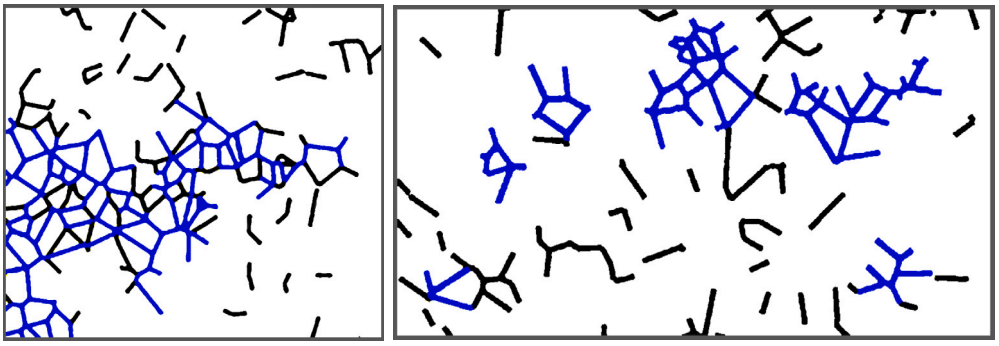

(a) S-max, high CSC to ISC ratio (b) S-max, low CSC to ISC ratio

Fig. A.22. Typical rGO inclusions (black) and nanocracks (blue) local patterns at S-max reference configuration at (a) high and (b) low CSC to ISC ratio.

More results of the corresponding 2D simulation, including the random, S-min, S-max reference configurations of rGO inclusions, and gif-animations of the 2-dimension IFN development can be found on the web host [69].

References

[1] X. Zhang, N. Zhao, C. He, The superior mechanical and physical properties of nanocarbon reinforced bulk composites achieved by architecture design - a review, Prog. Mater. Sci. 113 (2020) 100672, https://doi.org/10.1016/j.pmatsci.2020.100672.

[2] Y. Wu, F. Ma, J. Qu, T. Qi, Enhanced mechanical and piezoelectric properties of BCZT-CuY/rGO-based nanogenerator for tiny energy harvesting, Mater. Lett. 231 (2018) 20–23, https://doi.org/10.1016/j.matlet.2018.07.102.

[3] E. Borodin, A.P. Jivkov, A.G. Sheinerman, M.Y. Gutkin, Optimisation of rGO-enriched nanoceramics by combinatorial analysis, Mater. Des. 212 (2021) 110191, https://doi.org/10.1016/j.matdes.2021.110191.

[4] A.G. Sheinerman, N.F. Morozov, M.Y. Gutkin, Effect of grain boundary sliding on fracture toughness of ceramic/graphene composites, Mech. Mater. 137 (2019) 103126, https://doi.org/10.1016/j.mechmat.2019.103126.

[5] O.Y. Kurapova, O.V. Glumov, I.V. Lomakin, S.N. Golubev, M.M. Pivovarov, J.V. Krivolapova, V.G. Konakov, Microstructure, conductivity and mechanical properties of calcia stabilized zirconia ceramics obtained from nanosized precursor and reduced graphene oxide doped precursor powders, Ceram. Int. 44 (2018) 15464–15471, https://doi.org/10.1016/j.ceramint.2018.05.202.

[6] O.Y. Kurapova, A.G. Glukharev, O.V. Glumov, M.Y. Kurapov, E.V. Boltynjuk, V.G. Konakov, Structure and electrical properties of YSZ-rGO composites and YSZ ceramics, obtained from composite powder, Electrochim. Acta 320 (2019) 134573, https://doi.org/10.1016/j.electacta.2019.134573.

[7] L. Hu, W. Wang, Q. He, A. Wang, C. Liu, T. Tian, H. Wang, Z. Fu, Preparation and characterization of reduced graphene oxide-reinforced boron carbide ceramics by self-assembly polymerization and spark plasma sintering, J. Eur. Ceram. Soc. 40 (2020) 612–621, https://doi.org/10.1016/j.jeurceramsoc.2019.10.036.

[8] C. Song, Y. Liu, F. Ye, J. Wang, L. Cheng, Microstructure and electromagnetic wave absorption property of reduced graphene oxide-SiCnw/SiBCN composite ceramics, Ceram. Int. 46 (2020) 7719–7732, https://doi.org/10.1016/j.ceramint.2019.11.275.

[9] R. Zhou, L. Liao, Z. Chen, L. Zhong, X. Xu, Y. Han, Y. Zhong, Y. Zheng, R. Yao, Fabrication of monolithic rGO/SiC(O) nanocomposite ceramics via precursor (polycarbosilane-vinyltriethoxysilane-graphene oxide) route, Ceram. Int. 44 (2018) 14929–14934, https://doi.org/10.1016/j.ceramint.2018.05.084.

[10] L. Zhou, J. Qiu, X. Wang, H. Wang, Z. Wang, D. Fang, Z. Li, Mechanical and dielectric properties of reduced graphene oxide nanosheets/alumina composite ceramics, Ceram. Int. 46 (2020) 1–7, https://doi.org/10.1016/j.ceramint.2020.04.293.

[11] M. Li, W. Wang, Q. He, A. Wang, L. Hu, Z. Fu, Reduced-graphene-oxide-reinforced boron carbide ceramics fabricated by spark plasma sintering from powder mixtures obtained by heterogeneous co-precipitation, Ceram. Int. 45 (2019) 16496–16503, https://doi.org/10.1016/j.ceramint.2019.05.183.

[12] A. Gallardo-López, I. Márquez-Abril, A. Morales-Rodríguez, A. Muñoz, R. Poyato, Dense graphene nanoplatelet/yttria tetragonal zirconia composites: processing, hardness and electrical conductivity, Ceram. Int. 43 (2017) 11743–11752, https://doi.org/10.1016/j.ceramint.2017.06.007.

[13] N.W. Solís, P. Peretyagin, R. Torrecillas, A. Fernández, J.L. Menéndez, C. Mallada, L.A. Díaz, J.S. Moya, Electrically conductor black zirconia ceramic by SPS using graphene oxide, J. Electroceram. 38 (2017) 119–124, https://doi.org/10.1007/s10832-017-0076-z.

[14] Y. Cheng, Y. Liu, Y. An, N. Hu, High thermal-conductivity rGO/ZrB_2-SiC ceramics consolidated from ZrB_2-SiC particles decorated GO hybrid foam with enhanced thermal shock resistance, J. Eur. Ceram. Soc. 40 (2020) 2760–2767, https://doi.org/10.1016/j.jeurceramsoc.2020.03.029.

[15] Y. Huang, D. Jiang, X. Zhang, Z. Liao, Z. Huang, Enhancing toughness and strength of SiC ceramics with reduced graphene oxide by HP sintering, J. Eur. Ceram. Soc. 38 (2018) 4329–4337, https://doi.org/10.1016/j.jeurceramsoc.2018.05.033.

[16] P. Wu, H. Lv, T. Peng, D. He, S. Mu, Nano conductive ceramic wedged graphene composites as highly efficient metal supports for oxygen reduction, Sci. Rep. 4 (2014), https://doi.org/10.1038/srep03968.

[17] C.M. Hussain, S. Thomas, Handbook of Polymer and Ceramic Nanotechnology, Springer, 2021.

[18] M. Jakubczak, A.M. Jastrzębska, A review on development of ceramic-graphene based nanohybrid composite systems in biological applications, Front. Chem. 9 (2021), https://doi.org/10.3389/fchem.2021.685014.

[19] P. Sharma, G. Sharma, R. Punia, Graphene: A Prime Choice for Ceramic Composites, Elsevier, 2022, pp. 417–435.

[20] H. Zhao, H. Xing, Q. Lai, Y. Zhao, Q. Chen, B. Zou, Additive manufacturing of graphene oxide/hydroxyapatite bioceramic scaffolds with reinforced osteoinductivity based on digital light processing technology, Mater. Des. 223 (2022), https://doi.org/10.1016/j.matdes.2022.111231.

[21] Q. Lin, H. Chen, G. Xiao, M. Yi, Z. Chen, J. Zhang, C. Xu, J. Wu, Effect of graphene nanoplatelets on the mechanical properties and cutting performance of alumina nanocomposite ceramic tools prepared using the sps-hf dual sintering method, Ceram. Int. 48 (2022) 19240–19249, https://doi.org/10.1016/j.ceramint.2022.03.216.

[22] E. Cui, J. Zhao, X. Wang, Z. Sun, Improved fracture resistance and toughening mechanisms of gnps reinforced ceramic composites, Ceram. Int. 48 (2022) 24687–24694, https://doi.org/10.1016/j.ceramint.2022.05.115.

[23] M.A. Meyers, K.K. Chawla, Mechanical Behaviour of Materials, 2009.

[24] W. Wang, S. Dai, X. Li, J. Yang, D.J. Srolovitz, Q. Zheng, Measurement of the cleavage energy of graphite, Nat. Commun. 6 (2015) 7853, https://doi.org/10.1038/ncomms8853.

[25] H. Jiang, F. Jiang, D. Hu, R. Wang, J. Lu, B. Li, Numerical modeling of compressive failure mechanisms in ceramic materials at high strain rates, Comput. Methods Appl. Mech. Eng. 347 (2019) 806–826, https://doi.org/10.1016/j.cma.2019.01.006, https://www.sciencedirect.com/science/article/pii/S0045782519300106.

[26] P.D. Zavattieri, P.V. Raghuram, H.D. Espinosa, A computational model of ceramic microstructures subjected to multi-axial dynamic loading, J. Mech. Phys. Solids 49 (2001) 27–68, https://doi.org/10.1016/S0022-5096(00)00028-4, https://www.sciencedirect.com/science/article/pii/S0022509600000284.

[27] P.D. Boom, O. Kosmas, L. Margetts, A.P. Jivkov, A geometric formulation of linear elasticity based on discrete exterior calculus, Int. J. Solids Struct. 236–237 (2022) 111345, https://doi.org/10.1016/j.ijsolstr.2021.111345, https://www.sciencedirect.com/science/article/pii/S0020768321004212.

[28] K. Berbatov, P.D. Boom, A.L. Hazel, A.P. Jivkov, Diffusion in multi-dimensional solids using forman's combinatorial differential forms, Appl. Math. Model. 110 (2022) 172–192, https://doi.org/10.1016/j.apm.2022.05.043, https://www.sciencedirect.com/science/article/pii/S0307904X22002657.

[29] E.N. Borodin, A.P. Jivkov, Evolution of triple junctions network during severe plastic deformation of copper alloys— a discrete stochastic modelling, Philos. Mag. 100 (2020) 467–485, https://doi.org/10.1080/14786435.2019.1695071.

[30] P. Louisette, Grain boundaries. From theory to engineering, https://doi.org/10.1007/978-94-007-4969-6, 2013.

[31] M. Frary, C.A. Schuh, Connectivity and percolation behaviour of grain boundary networks in three dimensions, Philos. Mag. 85 (2005) 1123–1143, https://doi.org/10.1080/14786430412331323564, http://www.tandfonline.com/doi/abs/10.1080/14786430412331323564.

[32] R. Quey, Neper, https://neper.info/index.html, 2022.

[33] F. Aurenhammer, Voronoi diagrams - a survey of a fundamental data structure, ACM Comput. Surv. 23 (1991) 345–405.

[34] F. Aurenhammer, R. Klein, D.-T. Lee, Voronoi Diagrams and Delaunay Triangulations, World Scientific Publishing Company, 2013.

[35] D. Rabbe, Computer Simulations in Materials Science: the Simulation of Materials Microstructure and Properties, Wiley-VCH, Weinheim, 2004.
[36] D. Kozlov, Combinatorial Algebraic Topology, 2008.
[37] R. Fritsch, R. Piccinini, Cellular Structures in Topology, 1990.
[38] B. Bollobas, Modern Graph Theory, 1998.
[39] R. Durrett, Random Graph Dynamics, 2010.
[40] e. a. Borodin, Elijah, MATERIA project, http://materia.team/index.html, 2022.
[41] L.J. Grady, J.R. Polimeni, Discrete Calculus, 2010.
[42] P. van Mieghem, Graph Spectra for Complex Networks, 2011.
[43] J. Friedman, Computing betti numbers via combinatorial laplacians, Algorithmica (New York) 21 (1998) 331–346, https://doi.org/10.1007/PL00009218.
[44] S. Zhu, E. Borodin, A.P. Jivkov, Topological characteristics of grain boundary networks during severe plastic deformations of copper alloys, Acta Mater. 259 (2023) 119290, https://doi.org/10.1016/j.actamat.2023.119290, https://www.sciencedirect.com/science/article/pii/S1359645423006201.
[45] G.S. Rohrer, H.M. Miller, Topological characteristics of plane sections of polycrystals, Acta Mater. 58 (2010) 3805–3814.
[46] O. Knill, On Helmholtz free energy for finite abstract simplicial complexes, arXiv: 1703.06549, 2017, http://arxiv.org/abs/1703.06549.
[47] O. Bushuev, Polyhedral Cell Complex (PCC) analyser tool, https://github.com/PRISBteam/Voronoi_PCC_Analyser, 2022.
[48] E. Borodin, Polytopal Cell Complex (PCC) processing design code, https://github.com/PRISBteam/PCC_Processing_Design, 2024.
[49] E. Borodin, Polyhedral Cell Complex (PCC) fracture kinetic code, https://github.com/elbor7/DFK_code, 2022.
[50] E. Borodin, O. Bushuev, A. Barroso, PRISB project codes, https://github.com/PRISBteam, 2024.
[51] J. Benoit, G.e. Gael, Eigen library, https://eigen.tuxfamily.org/, 2022.
[52] Y.e. Qiu, Sparse eigenvalue computation toolkit as a redesigned ARPACK (SPECTRA), https://spectralib.org/, 2022.
[53] S. Pei, H.M. Cheng, The reduction of graphene oxide, Carbon 50 (2012) 3210–3228, https://doi.org/10.1016/j.carbon.2011.11.010.
[54] A.H. Tavakoli, P.S. Maram, S.J. Widgeon, J. Rufner, K. van Benthem, S. Ushakov, S. Sen, A. Navrotsky, Amorphous alumina nanoparticles: structure, surface energy, and thermodynamic phase stability, J. Phys. Chem. C 117 (2013) 17123–17130, https://doi.org/10.1021/jp405820g.
[55] Z. Dou, Z. Chen, N. Li, S. Yang, Z. Yu, Y. Sun, Y. Li, B. Liu, Q. Luo, T. Ma, L. Liao, Z. Liu, P. Gao, Atomic mechanism of strong interactions at the graphene/sapphire interface, Nat. Commun. 10 (2019) 5013, https://doi.org/10.1038/s41467-019-13023-6.
[56] S. Zhu, E. Borodin, A.P. Jivkov, Triple junctions network as the key pattern for characterisation of grain structure evolution in metals, Mater. Des. 198 (2021) 109352, https://doi.org/10.1016/j.matdes.2020.109352.
[57] R.R. Forman, Bochner's method for cell complexes and combinatorial Ricci curvature, Discrete Comput. Geom. 29 (2003) 323–374, https://doi.org/10.1007/s00454-002-0743-x.
[58] E. Borodin, A. Morozova, V. Bratov, A. Belyakov, A. Jivkov, Experimental and numerical analyses of microstructure evolution of cu-cr-zr alloys during severe plastic deformation, Mater. Charact. 156 (2019) 109849, https://doi.org/10.1016/j.matchar.2019.109849, https://www.sciencedirect.com/science/article/pii/S104458031931383X.
[59] C.E. Shannon, A mathematical theory of communication, Bell Syst. Tech. J. 27 (1948) 379–423, https://doi.org/10.1002/j.1538-7305.1948.tb01338.x, https://ieeexplore.ieee.org/document/6773024.
[60] L.M. Martyushev, V.D. Seleznev, Maximum entropy production principle in physics, chemistry and biology, Phys. Rep. 426 (2006) 1–45, https://doi.org/10.1016/j.physrep.2005.12.001, https://linkinghub.elsevier.com/retrieve/pii/S0370157305004813.
[61] M.A.G. Viana, Symmetry Studies: An Introduction to the Analysis of Structured Data in Applications, Cambridge Series in Statistical and Probabilistic Mathematics, 2008.
[62] M. Frary, C.A. Schuh, Percolation and statistical properties of low- and high-angle interface networks in polycrystalline ensembles, Phys. Rev. B, Condens. Matter Mater. Phys. 69 (2004) 134115, https://doi.org/10.1103/PhysRevB.69.134115, https://link.aps.org/doi/10.1103/PhysRevB.69.134115.
[63] L. Wei, H. Jin Sim, H. Cao, Y. Chen, P. Xiao, Effect of reduced graphene oxide on the mechanical properties of rGO/Al_2O_3 composites, Ceram. Int. 48 (2022) 24021.
[64] M. Kukielski, W. Bulejak, P. Wiecinska, L. Stobinski, W. Slubowska, M. Szafran, Graphene-reinforced ceramics obtained by slip casting and pressureless sintering: interactions and stability of particles in aqueous environment, Open Ceram. 9 (2022), https://doi.org/10.1016/j.oceram.2022.100245.
[65] H. Porwal, S. Grasso, M.J. Reece, Review of graphene-ceramic matrix composites, Adv. Appl. Ceram. 112 (2013) 443–454, https://doi.org/10.1179/174367613X13764308970581.
[66] X. Wang, J. Zhao, E. Cui, Z. Sun, H. Yu, Nano/microstructures and mechanical properties of al2o3-wc-tic ceramic composites incorporating graphene with different sizes, Mater. Sci. Eng. A 812 (2021), https://doi.org/10.1016/j.msea.2021.141132.
[67] B. Ratzker, M. Sokol, Exploring the capabilities of high-pressure spark plasma sintering (hpsps): a review of materials processing and properties, Mater. Des. 233 (2023), https://doi.org/10.1016/j.matdes.2023.112238.
[68] Q. Zhang, H. Liu, T. Qiao, P.J. Withers, P. Xiao, Simple and efficient densification of sicf/sic composites by gradated concentration polymer infiltration and pyrolysis, Mater. Sci. Eng. A 874 (2023), https://doi.org/10.1016/j.msea.2023.145065.
[69] E. Borodin, MATERIA project 2D examples, https://materia.team/assets/simulations/rgo.html, 2023.